

PNNL-36491

# Development Results on Replacement Materials for Current Scarce or High Supply Chain Risk Materials

M3CR-22PN0401015

August 2024

Carolyn Burns	Ankit Roy
Steven Livers	Benjamin Lund
Subhashish Meher	Mohan Nartu
Asif Mahmud	Tianhao Wang
David Garcia	Jorge Dos Santos
Pratikshya Meher	Chinthaka Silva
Thomas Hartmann	
Isabella van Rooyen	



## DISCLAIMER

This report was prepared as an account of work sponsored by an agency of the United States Government. Neither the United States Government nor any agency thereof, nor Battelle Memorial Institute, nor any of their employees, makes **any warranty, express or implied, or assumes any legal liability or responsibility for the accuracy, completeness, or usefulness of any information, apparatus, product, or process disclosed, or represents that its use would not infringe privately owned rights.** Reference herein to any specific commercial product, process, or service by trade name, trademark, manufacturer, or otherwise does not necessarily constitute or imply its endorsement, recommendation, or favoring by the United States Government or any agency thereof, or Battelle Memorial Institute. The views and opinions of authors expressed herein do not necessarily state or reflect those of the United States Government or any agency thereof.

PACIFIC NORTHWEST NATIONAL LABORATORY  
*operated by*  
BATTELLE  
*for the*  
UNITED STATES DEPARTMENT OF ENERGY  
*under Contract DE-AC05-76RL01830*

Printed in the United States of America

Available to DOE and DOE contractors from  
the Office of Scientific and Technical Information,  
P.O. Box 62, Oak Ridge, TN 37831-0062

[www.osti.gov](http://www.osti.gov)

ph: (865) 576-8401

fox: (865) 576-5728

email: [reports@osti.gov](mailto:reports@osti.gov)

Available to the public from the National Technical Information Service  
5301 Shawnee Rd., Alexandria, VA 22312

ph: (800) 553-NTIS (6847)

or (703) 605-6000

email: [info@ntis.gov](mailto:info@ntis.gov)

Online ordering: <http://www.ntis.gov>

# **Development Results on Replacement Materials for Current Scarce or High Supply Chain Risk Materials**

M3CR-22PN0401015

August 2024

Carolyne Burns  
Steven Livers  
Subhashish Meher  
Asif Mahmud  
David Garcia  
Pratikshya Meher  
Thomas Hartmann  
Isabella van Rooyen

Ankit Roy  
Benjamin Lund  
Mohan Nartu  
Tianhao Wang  
Jorge Dos Santos  
Chinthaka Silva

Prepared for  
the U.S. Department of Energy  
under Contract DE-AC05-76RL01830

Pacific Northwest National Laboratory  
Richland, Washington 99354

## Summary

In September 2020, the U.S. government issued an executive order to address the threat to the domestic supply chain from its reliance on critical minerals (CMs) from foreign competitors and to support the domestic mining and processing industry. The Advanced Materials and Manufacturing Technology (AMMT) program is addressing this executive order by evaluating advanced manufacturing (AM) and its impact on the demands of CMs for energy production in general and how the deployment of AM in nuclear energy will support the projected goals of the Paris Accord and further a net-zero carbon economy (NZE) by 2050. Two strategic reports were previously prepared by the AMMT program and identified two areas for more detailed exploration: (1) the replacement of high-risk CMs such as cobalt and niobium by more abundant minerals and (2) the minimization and utilization of CM waste streams.

This work describes development activities of the replacement of high risks CMs. The design of nuclear materials without critical elements as alloying elements is a part of the nuclear materials strategy to overcome the critical minerals scarcity. In this report, two approaches are evaluated, namely (1) replacement of critical elements as alloying elements in nuclear materials, and (2) the design of new alloys that do not contain critical minerals as an alloying element.

For the first approach, Inconel 617 (IN617) has been selected as an alloy system to substitute its high Co concentration using noncritical Mn. Inconel 617 is an alloy system that has been recently ASME-code certified for high-temperature nuclear systems (US Office of Nuclear Energy, 2020), therefore was used as a feasibility study. A computational feasibility study of compositional changes to IN617 with simulation generation of stress-strain curves determined the impact that Co replacement with Mn has on the alloy's mechanical properties (e.g., tensile strength). For select composition, phase diagrams were calculated and upon promising and similar results compared to the original alloy, experimental verification was performed. The phase diagrams and tensile simulations suggest that Mn substituted for Co will yield similar tensile strength and phase stability.

The composition with the best combination of simulated oxygen penetration and tensile strength was down selected for experimental fabrication and characterization. Two different fabrication methods were used to fabricate alloy samples, 1) casting and 2) friction stir consolidation and alloying. The samples were then characterized using SEM-EDS, XRD (casting alloy only) and Vickers hardness. IN617-M1 shows considerable promise as a material, particularly when subjected to advanced processing methods like friction stir alloying (FSA) due to the grain refinement as an additional strengthening mechanism.

For the second approach evaluated herein, multi objective Bayesian optimization (MOBO) techniques were employed to design novel alloys for nuclear applications that do not contain the critical minerals nickel and cobalt while maximizing alloy yield strength and hardness. The material system within which new compositions were developed for this study is Fe-Cr-Cu-Al-Nb-Ta-Ti-V-Zr-Mo-W-Mn. Predictions made through MOBO need to be verified by conducting simulations using molecular dynamics and by experimentally producing the alloys and measuring their hardness and yield strength values.

## Acknowledgments

The research presented here was supported by the Advanced Materials and Manufacturing Technology (AMMT) program of the DOE Office of Nuclear Energy. PNNL is a multi-program national laboratory operated for the U.S. Department of Energy (DOE) by Battelle Memorial Institute under Contract No. DE-AC05-76RL01830. Heather Culley is thanked for her editorial review of this report. Richard Daniel is thanked for his technical review of the report and its contents. The contribution of Mr. Alan Schemer-Kohrn is acknowledged for his assistance in XEDS analysis of the as-cast IN617-M1 sample.

## Acronyms and Abbreviations

Al ppt	aluminum Precipitates
AM	advance manufacturing
AMMT	Advanced Materials and Manufacturing Technology
ASME	American Society of Mechanical Engineers
BSE	backscattered electron
CM	critical minerals
DOE	U.S. Department of Energy
EBSD	electron backscatter diffraction
EDS	energy dispersive spectroscopy
fcc	face-centered cubic unit cell
FSA	friction stir alloying
FSC	friction stir consolidation
FSW	friction stir welding
GAN	generative adversarial networks
GB ppt	grain boundary precipitates
GFR	gas cooled fast reactor
HEA	high entropy alloy
MD	molecular dynamics
ML	machine learning
Mn ppt	manganese precipitates
MOBO	multi objective Bayesian optimization
MSR	molten salt reactor
NSGA	non-dominate sorting genetic algorithm
PNNL	Pacific Northwest National Laboratory
SEM	scanning electron microscopy
VHTR	very high-temperature gas-cooled reactor

## Contents

Summary .....	ii
Acknowledgments .....	iii
Acronyms and Abbreviations.....	iv
1.0 Introduction .....	1
1.1 Background.....	1
1.2 Strategy for Decreasing Nuclear Material Vulnerability Due to CMs.....	2
1.3 Scope of This Report .....	2
2.0 Replacement of Critical Elements as Alloying Elements in Nuclear Materials .....	4
2.1 Molecular Dynamics Simulations .....	4
2.1.1 Tensile Simulations .....	4
2.1.2 Oxidation Simulations.....	7
2.1.3 Simulation Results.....	8
2.2 Phase Diagram Calculations .....	9
2.3 Experimental Validation of the MD Simulations.....	11
2.3.1 Casting Using an Induction Furnace.....	12
2.3.2 Friction Consolidation and Solid Phase Alloying .....	14
2.4 Characterization Results and Discussion .....	16
2.4.1 Characterization Methods.....	16
2.4.2 Characterization Results of IN617-M1 Cast Alloy .....	17
2.4.3 Optical Imaging and Vickers Hardness IN617-M1 Cast Alloy.....	18
2.4.4 XRD IN617-M1 Cast Alloy .....	19
2.4.5 Compositional Analysis IN617-M1 Cast Alloy .....	19
2.4.6 IN617-M1 Friction Stir Alloying .....	21
2.4.7 Optical Imaging and Hardness .....	21
2.4.8 Microstructural Analysis of FSA IN617-M1 Run#1 .....	22
2.4.9 Compositional Analysis IN617-M1 Run #1.....	23
2.4.10 Microstructural Analysis of FSA IN617-M1 Run#2 .....	24
2.5 MD Performance Conclusion .....	25
3.0 New Alloy Development Using Multi Objective Bayesian Optimization .....	27
3.1 Design Strategy .....	27
3.2 Hardness and Yield Strength Model.....	28
3.3 Multi Objective Bayesian Optimization .....	31
3.4 Next Actions.....	33
4.0 Conclusions and Recommendations .....	34
5.0 Reports, Publications and Presentations .....	A.1
6.0 References.....	A.2
Appendix A Datasets Used for MOBO .....	A.1

## Figures

Figure 1.	Schematic of the CM strategy for nuclear materials as developed during this study. ....	2
Figure 2.	(a) A typical FCC alloy relaxed in molecular dynamics for IN617. (b) Unidirectional tensile deformation executed along the x-direction. ....	5
Figure 3.	The stress-strain curve due to uniaxial loading in the x-direction for (a) IN617 and its five modifications: (b) IN617-M1, (c) IN617-M2, (d) IN617-M3, (e) IN617-M4, and (f) IN617-M5. IN617-M1 shows the best performance at both room temperature and 950 K. ....	6
Figure 4.	(a) Initial configuration of doubled layered oxygen atoms over the alloy surface. (b) Formation of oxide layer 100 ps after the initiation of simulation. (c) A schematic representing the oxygen atoms penetration depth. ....	8
Figure 5.	Phase fraction versus temperature plot for IN617 simulated using TCFE13 database and Thermo-Calc 2024a. ....	9
Figure 6.	Phase fraction versus temperature plot obtained from Rai et al. (2017). ....	10
Figure 7.	SEM image showing the presence of $\pi$ phase in IN617 alloy. Image reproduced from Wang et al., (2023). ....	10
Figure 8.	Phase fraction versus temperature plot for 617-M1 simulated using TCFE13 database and Thermo-Calc 2024a. ....	11
Figure 9.	Phase fraction versus temperature plot for 617-M2 simulated using TCFE13 database and Thermo-Calc 2024a. ....	11
Figure 10.	4N to 5N elemental purity pure elements, left. IN617 filaments and chips, middle and alumina crucible with pure elements and IN617 ready for casting. ....	12
Figure 11.	Pure metal components and Inconel 617 chips pressed into pellets. ....	12
Figure 12.	MTI 25 kW Induction furnace with induction coil, left, coil, insulation, and internal crucible setup used for alloying new metal compositions, right. ....	13
Figure 13.	Temperature profile used to melt Inconel 617-M1. ....	13
Figure 14.	IN617-M1 ingot formed, max temperature of 1740°C, from left to right - Side, Bottom, and Top of ingot. ....	14
Figure 15.	A mixture of Inconel 617 chips and pure metal alloying additions. ....	14
Figure 16.	Friction consolidation and solid phase alloying setup. ....	15
Figure 17.	Machine data of tool position (Z position), loading force (Z-axis force), tool/chip interface temperature, rotation rate and spindle torque for Run #1 and 2. ....	16
Figure 18.	Top- and bottom view of consolidated and alloyed chips for Run #1 and #2. ....	16
Figure 19.	Optical micrographs of as-cast IN617-M1 sample with indents for Vickers hardness measurement. ....	18
Figure 20.	Comparison of IN617-Co 12.5 wt% and the modified IN617-M1-Co 2.5 wt% alloy sample from casting at ~1700°C using and induction furnace.	

	Peaks correspond to the Si standard (NIST SRM 640g) and fcc phase are denoted by red and blue tick marks, respectively. ....	19
Figure 21.	XEDS compositional mapping of the backscattered electron micrographs of IN617-M1 cast alloy. ....	20
Figure 22.	Optical micrographs and Vickers hardness FSA IN617-M1 Run#1 sample, (a) OM with indents and, (b) Vickers hardness as a function of data points.....	22
Figure 23.	(a-c) show BSE micrograph of FSA IN617-M1 Run#1 sample, (d) shows the inverse pole figure of this alloy. ....	23
Figure 24.	XEDS compositional mapping of the backscattered electron micrographs of IN617-M1 Run#1 FSA sample. ....	24
Figure 25.	(a-b) shows the BSE images of FSA IN617-M1 Run#2 sample that shows the chemical inhomogeneity through the variation in image contrast.....	24
Figure 26.	(a-b) XEDS compositional mapping of the backscattered electron micrographs of FSA IN617-M1 Run #2 sample. The chemical inhomogeneity is pronounced in this sample.....	25
Figure 27.	Multi objective Bayesian optimization framework. ....	28
Figure 28.	Hardness versus yield strength of the alloys in original training data represented using yellow dots and new compositions suggested by Bayesian optimization represented using blue dots. The solid blue line represents the alloys in the Pareto front.....	32

## Tables

Table 1.	Elemental composition of IN617 and its modified compositions. ....	4
Table 3.	The interatomic potentials used to define the interactions of all nine elements for oxidation simulations of IN617 and its modifications. ....	7
Table 4.	Average oxygen penetration depth and tensile strength for IN617 and its modifications. Only Co and Mn elemental compositions are noted for reference. ....	8
Table 5.	Metal masses used for friction consolidation and solid phase alloying runs. ....	14
Table 6.	Critical parameters for friction consolidation of 617M1 alloy chips.....	15
Table 7.	Vickers hardness values for the as-cast IN617-M1 alloy for the indentation regions marked in Figure 19. ....	18
Table 8.	Elemental composition of regions highlighted in Figure 21 IN617-M1 composition included for comparison. ....	21
Table 9.	Summary of Vickers hardness values measured for both casting and friction stir alloying. ....	21
Table 10.	The chemical composition of the IN617-M1 Run#1 FSA sample corresponding to Figure 24. ....	24
Table 11.	Comparison of MD performance compared to experimental data.....	25
Table 12.	Formulas used to compute input features of hardness and yield strength models. ....	29
Table 13.	Performance of hardness and yield strength models.....	31

Table 14. Details of 3 composition on the Pareto front and their predicted hardness and yield strength (YS).....33

## 1.0 Introduction

In September 2020, the U.S. government issued an executive order to address the threat to the domestic supply chain from its reliance on critical minerals (CMs) from foreign competitors and to support the domestic mining and processing industry (DOE 2021). In this context, a national strategy on CMs was developed, which had an impact on the U.S. Department of Energy's (DOE's) vision for the decade of 2021–2031. This vision embraces science and technology to re-establish U.S. competitiveness in the CM and material supply chains by (a) scientific innovation and technologies to ensure resilient and secure CMs and maintain a domestic material supply chain, (b) building a long-term minerals and materials innovation ecosystem to foster new capabilities to mitigate CM supply chain challenges, (c) increasing private sector adoption for sustaining the domestic CM supply chain, and (d) coordinating with international partners and federal agencies to diversify global supply chains and ensure the adoption of best practices for sustainable mining and processing (DOE 2021). The Advanced Materials and Manufacturing Technology (AMMT) program of the DOE Office of Nuclear Energy is addressing this executive order by evaluating advanced manufacturing (AM) and its impact on the demands of CMs for energy production in general and how the deployment of AM in nuclear energy will support the projected goals of the Paris Accord and further a net-zero carbon economy (NZE) by 2050. Two strategic reports have been issued by the AMMT to date (Hartmann et al., 2022, 2023), and detailed experimental design and execution have been the focus of the past year's work regarding (1) the replacement of high-risk CMs such as cobalt and niobium with more abundant minerals (this report) and (2) the minimization and utilization of CM waste streams (van Rooyen et al., 2024).

### 1.1 Background

The demand for metals and CMs will rapidly increase with international ambitions to address climate change, in which the current strategy is set up to comply with a 2°C scenario (cf. 2015 Paris Accord). Global material use will more than double, from 79 billion tons in 2011 to 167 billion tons in 2060. The projected growth in materials use, coupled with the environmental consequences of material extraction, processing, and waste, is likely to increase pressure on the resource bases of the planet's economies and jeopardize economic and social gains in well-being.

CMs are essential for a range of clean energy technologies, which are experiencing rapid growth due to global policies and business agendas in recent years. Record deployment of clean energy technologies such as solar photovoltaics and batteries is propelling unprecedented growth in CM markets, while electric car sales exceeded 10 million units in 2022. Energy storage systems experienced even more rapid growth, with capacity additions doubling in 2022 and wind power installations set to resume their upward trend. All of this has led to a significant increase in demand for CMs and increased supply pressure on all other industries. From 2017 to 2022, demand from the energy sector was the main factor behind a tripling in the overall demand for lithium, a 70% jump in demand for cobalt, and a 40% rise in demand for nickel. In 2022, the share of clean energy applications of the total demand reached 56% for lithium, 40% for cobalt, and 16% for nickel, up from 30%, 17%, and 6%, respectively, five years ago (IEA 2023).

Driven by rising demand and high prices, the market share of energy transition minerals doubled over the past five years, reaching USD 320 billion in 2022. Energy transition minerals, which used to be a small segment of the market, are now moving to center stage in the mining

and metals industry. A combination of volatile price movements, supply chain bottlenecks, and geopolitical concerns has created a mix of risks for secure and rapid energy transitions.

## 1.2 Strategy for Decreasing Nuclear Material Vulnerability Due to CMs

Figure 1 shows a schematic of the CM strategy for nuclear materials adapted from previous work (Hartmann et al., 2022). As a part of the U.S. DOE's focus on CMs, increasing manufacturing efficiency, identifying better substitutes, and improving the recycling and recovery of CMs are important aspects that need focus using both experimental and computational efforts. Experimental feasibility studies were identified as part of the strategy to decrease nuclear material vulnerability due to CM supply and economic impacts on the following elements: (1) Co, as a short-term (2020–2050) and medium-term (2025–2035) high supply risk, and (2) Ni, a near-critical material for near term, but a high critical material for the medium term (2025–2035).

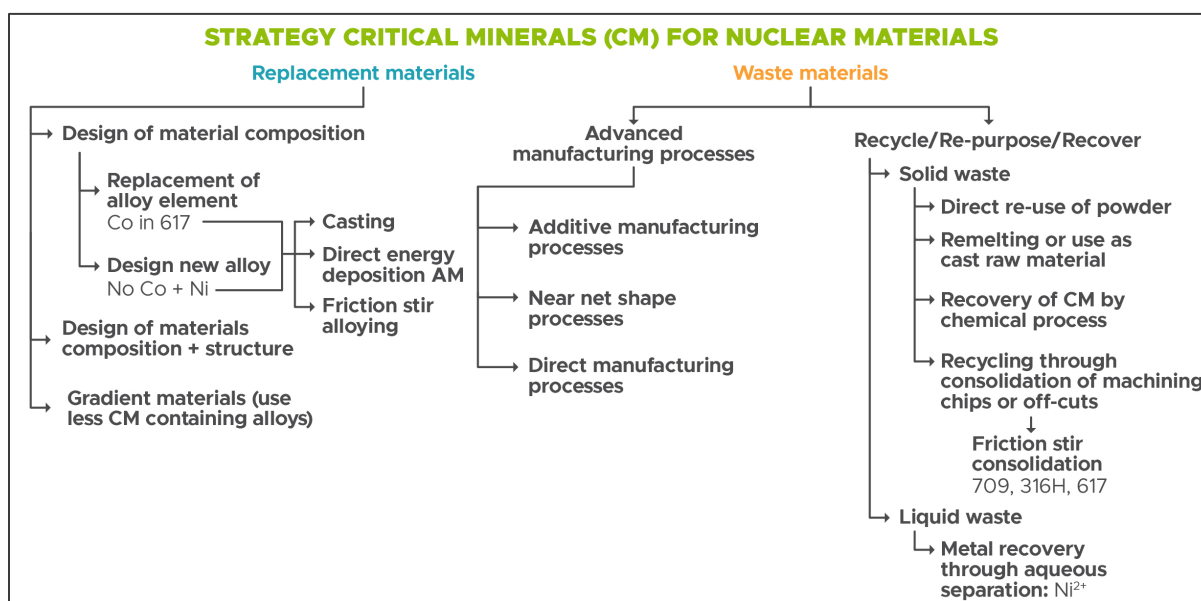


Figure 1. Schematic of the CM strategy for nuclear materials as developed during this study.

## 1.3 Scope of This Report

The design of nuclear materials without critical elements as alloying elements, is a part of the nuclear materials strategy to overcome the critical minerals scarcity. For this work, two approaches are evaluated namely (1) replacement of critical elements as alloying elements in nuclear materials (Section 2.0 of this report), and (2) the design of a new alloy that does not contain critical minerals as an alloying element (Section 3.0 of this report).

For the first approach, Inconel 617 has been selected as an alloy system to substitute its high Co concentration using noncritical Mn as the alloy system is also ASME-code certified for high-temperature nuclear systems under Boiler and Pressure Vessel Code (US Office of Nuclear Energy, 2020), please note the composition medication may result in new codification activities. Alloy 617 is considered to be used in molten salt reactor (MSR), gas-cooled fast reactor (GFR),

and very high-temperature gas-cooled reactor (VHTR) systems due to its desirable properties such as high mechanical strength, good oxidation and corrosion resistance and considerably low thermal expansion (Natesan and Tam, 2003), high phase stability preventing the formation of embrittling phases (e.g., sigma, mu, chi, or Laves phases) at elevated temperatures, and good weldability. IN617 is an austenitic Ni-Cr alloy with solution strengthening from the addition of Co (~12 wt.%) and Mo (~9 wt.%) leading to good creep strengths at temperatures >870°C. It also has Al (~1 wt.%) and a small amount of C (~0.06 wt.%) resulting Inconel 617 to have a good corrosion resistance and high mechanical strength (Totemeier and Tian, 2007), respectively. However, if internal Al<sub>2</sub>O<sub>3</sub> is formed, it can result in carburization producing unwanted carbides followed by the degradation of the alloy (McKee and Frank, 1981). As manganese (Mn) is identified as a noncritical mineral and can also form a protective layer (MnO<sub>2</sub>) supporting corrosion resistance of the material, Mn is suggested as a potential replacement for high Co concentration in IN617. Lower capture cross section towards thermal neutrons of Mn ( $13.3 \times 10^{-24} \text{ cm}^2$ ) compared to Co ( $37.3 \times 10^{-24} \text{ cm}^2$ ) also brings another advantage as an alloy component in structural materials for nuclear reactors.

In this report, a computational feasibility study of compositional changes to IN617 are presented. Compositional modifications were made by systematically substituting the Co concentration in IN617 for Mn generating a set of possible compositional modifications (Table 1). These computational studies include analysis of the effect of Mn addition and Co subtraction on strength and corrosion resistance at different atomic percentages and their phase diagram calculations. For the mechanical properties, tensile tests on cubic simulation cells have been performed to obtain the stress strain curve that reveal the effect of Co replacement with Mn on the tensile strength. Phase diagrams were calculated for a few compositions that showed promising results in the simulation evaluations.

The composition with the best combination of oxygen penetration and tensile strength was selected for experimental evaluation. Two different methods were used in this study to obtain alloy samples, 1) casting and 2) friction stir consolidation and alloying. The materials were then characterized using SEM-EDS, XRD (casting alloy only) and Vickers hardness.

For the second approach, multi objective Bayesian optimization (MOBO) techniques were employed to design new alloys that do not contain the critical minerals nickel and cobalt. The high entropy alloy (HEA) system within which new compositions were developed for this study is Fe-Cr-Cu-Al-Nb-Ta-Ti-V-Zr-Mo-W-Mn. MOBO was used to develop a new material composition with maximum yield strength and hardness not containing nickel and cobalt both known for their hardening properties.

## 2.0 Replacement of Critical Elements as Alloying Elements in Nuclear Materials

### 2.1 Molecular Dynamics Simulations

The six different elemental compositions simulated in this study are shown in Table 1. Molecular dynamics simulations of tensile strain were carried out in the extensively parallelized Large-scale Atomic/Molecular Massively Parallel Simulator (LAMMPS) package (Plimpton, 1995); OVITO (Stukowski, 2009) was used for visualization and data-processing. Figure 2 shows the visualization of the relaxed FCC supercell and the deformed supercell after tensile strain. The embedded-atom potentials (EAM) described by Zhou et al (2004) and long-range Lennard-Jones potential by Gröger et al. (2020) were used to define the interatomic potentials. The lattice was energy minimized using the conjugate-gradient method with an energy tolerance of  $10^{-15}$  eV and a force tolerance of  $10^{-15}$  eV/Å in LAMMPS.

Table 1. Elemental composition of IN617 and its modified compositions.

Material	Elemental wt.%										Reference
	C	Cr	Ni	Co	Mn	Mo	Ti	Al	Fe	Total	
IN617	0.06	21.6	53.6	12.5	0.0	9.5	0.3	1.2	0.9	99.66	Natesan and Tam (2003)
IN617-M1	0.06	26.6	53.6	2.5	5	9.5	0.3	1.2	0.9	99.66	1st modification
IN617-M2	0.06	24.1	53.6	7.5	2.5	9.5	0.3	1.2	0.9	99.66	2nd modification
IN617-M3	0.06	21.6	53.6	2.5	10	9.5	0.3	1.2	0.9	99.66	3rd modification
IN617-M4	0.06	21.6	53.6	7.5	5	9.5	0.3	1.2	0.9	99.66	4th modification
IN617-M5	0.06	21.6	53.6	10	2.5	9.5	0.3	1.2	0.9	99.66	5th modification

#### 2.1.1 Tensile Simulations

The alloy simulation was initialized with a face-centered cubic unit cell, fcc structure at 300 K under an isothermal-isobaric (NPT) ensemble for 50 ps. Periodic boundary conditions were applied in all the directions. Unidirectional tensile deformation was carried out at a strain rate of  $0.01 \text{ ps}^{-1}$  along the x-direction. The strain rate adopted here was previously employed for analyzing the deformation of AlCoCrFeNi HEA (Sharma and Balasubramanian, 2017) and Mo-Ta-Ti-W-Zr (Singh et al., 2018; Roy et al., 2022). The simulated strain rate is several orders of magnitude higher relative to experiments; this difference is necessitated by the timescales feasible in MD simulations (Wen et al., 2008).

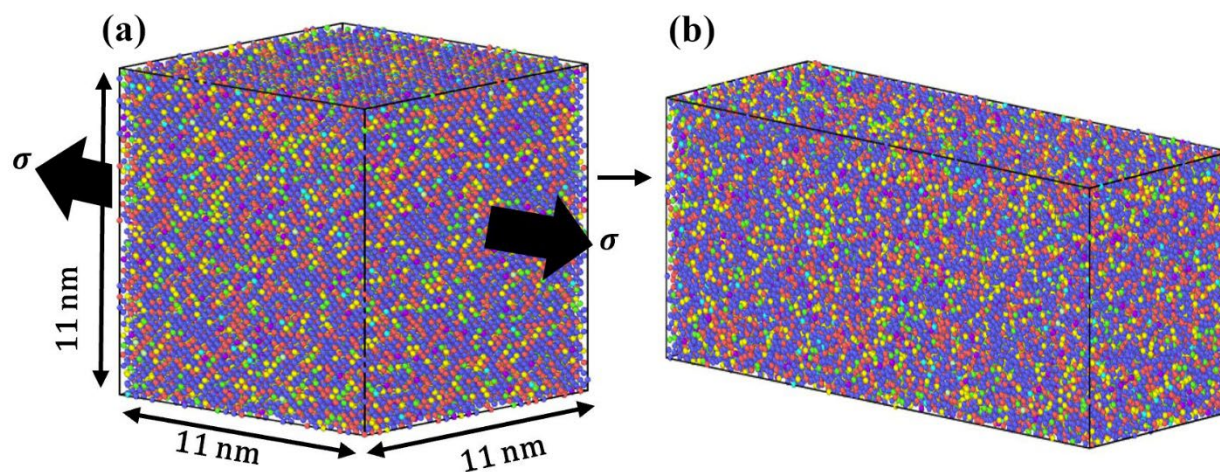


Figure 2. (a) A typical FCC alloy relaxed in molecular dynamics for IN617. (b) Unidirectional tensile deformation executed along the x-direction.

The results of the tensile simulations are shown in Figure 3. IN617-M1 possesses the highest strength at both room temperature and 950 K.

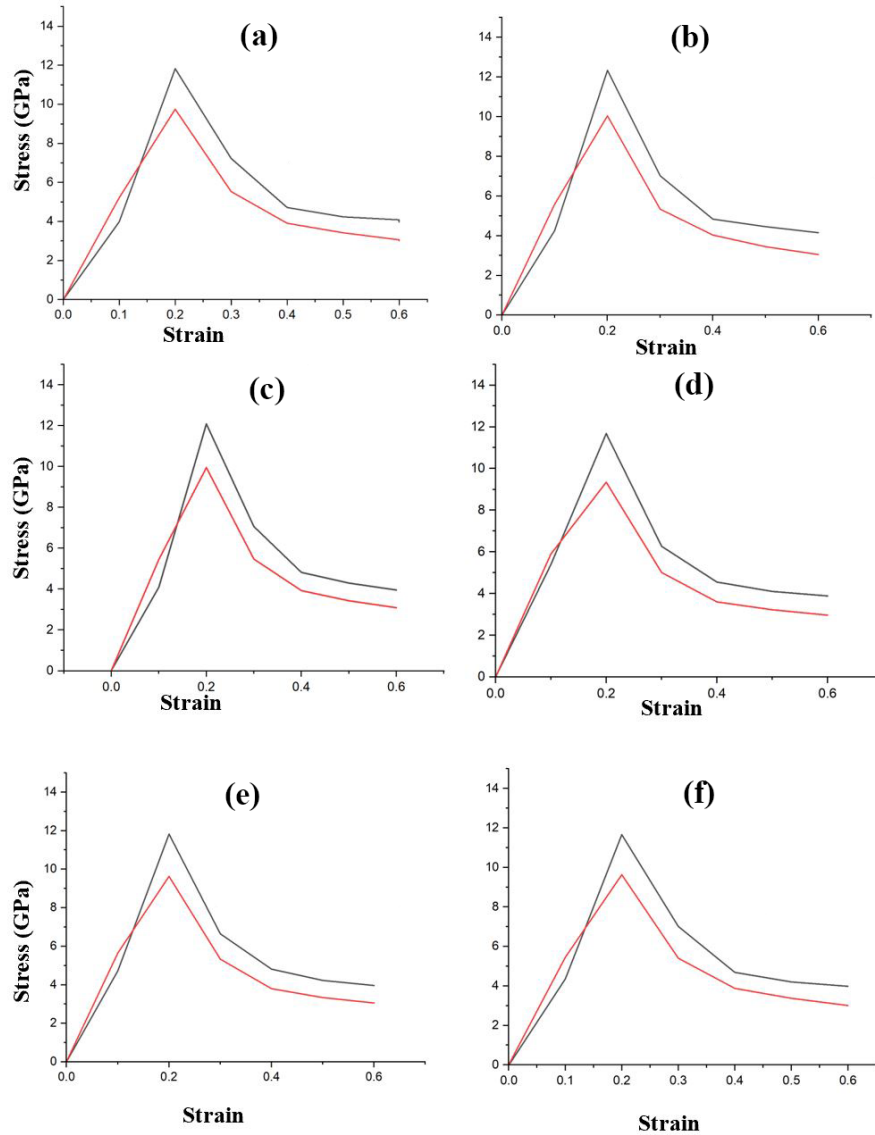


Figure 3. The stress-strain curve due to uniaxial loading in the x-direction for (a) IN617 and its five modifications: (b) IN617-M1, (c) IN617-M2, (d) IN617-M3, (e) IN617-M4, and (f) IN617-M5. IN617-M1 shows the best performance at both room temperature and 950 K.

In our study, MD simulations were conducted under tensile stress conditions to derive the yield strengths of various alloy modifications. These tensile strengths can be effectively correlated to hardness using several well-established relationships in the literature. One commonly cited relationship is

$$H_V \approx 3. \sigma_y \quad 1$$

where  $H_V$  represents the Vickers hardness and  $\sigma_y$  denotes the yield strength (An et al., 2010; Zhang et al., 2011; Li and Ebrahimi, 2003). Hardness testing is fundamentally a surface phenomenon, quantifying the localized deformation around the indenter on the material's surface (Biotman, 2017). In contrast, tensile deformation assessments provide insights into the

material properties at the bulk level, offering a more comprehensive evaluation of the material's overall strength.

However, tensile testing is both time-consuming and cost-intensive compared to hardness measurements. Consequently, for experimental validation in this study, we opted for hardness measurements due to their efficiency and practicality.

The relative order of alloy strengths determined from tensile simulations is expected to correspond with the order of the hardness values because of the linear proportionality between yield strength and hardness. Thus, while the MD simulations assessed the yield strengths for six different alloy modifications, the experimental validation focused on hardness measurements of the alloy predicted to have the highest strength.

## 2.1.2 Oxidation Simulations

To simulate the interaction between oxygen and the metals present in the alloy, we employed a set of interatomic interactions detailed in Table 2. The simulation cell, with dimensions of 5 nm × 5 nm × 5 nm as illustrated in Figure 2, served as the framework for our study. To mimic the formation of an oxide layer, we initially introduced a 2-atomic-layer-thick oxygen layer onto the alloy surface, depicted in Figure 3 (a). The systems, including the IN617 alloy and its variations, underwent initialization at 500 K within the isothermal-isobaric (NPT) ensemble, followed by a 100 ps equilibration period. During this equilibration, oxygen atoms diffused through the alloy surface into its bulk, culminating in the formation of an oxide layer of specific thickness, as demonstrated in Figure 3 (b) and (c). The average oxygen penetration depth is calculated as

$$d = \frac{d_1 + d_2 + d_3 + \dots + d_n}{n} = \frac{\sum_{i=1}^n d_i}{n} \quad 2$$

Where  $d_1, d_2, \dots, d_n$ , are the penetration depth from the surface, of each oxygen atom  $O_1, O_2, O_3, \dots, O_n$ .

**Table 2.** The interatomic potentials used to define the interactions of all nine elements for oxidation simulations of IN617 and its modifications.

Pair/group	Ref.	Interatomic potential type
Cr-Ni-Co-Mo-Ti-Al-Fe	Zhou et al. (2004)	EAM
Cr-Mn, Ni-Mn, Co-Mn, Fe-Mn, Mn-Mn	Groger et al. (2020)	Long-range Lennard-Jones potential
Cr-O	Minervini et al. (1999)	Buckingham potential
Ni-O	Restrepo et al. (2022)	Buckingham potential
Co-O	Hermet et al. (2010)	Buckingham potential
Mn-O	Maphanga et al. (2009)	Buckingham potential
Mo-O	Rajaramakrishna et al. (2020)	Buckingham potential
Ti-O	Bandura and Kubicki (2003)	Buckingham potential
Al-O	Georgieva et al. (2009)	Buckingham potential
Fe-O	Restrepo et al. (2022)	Buckingham potential
O-O	Minervini et al. (1999)	Buckingham potential

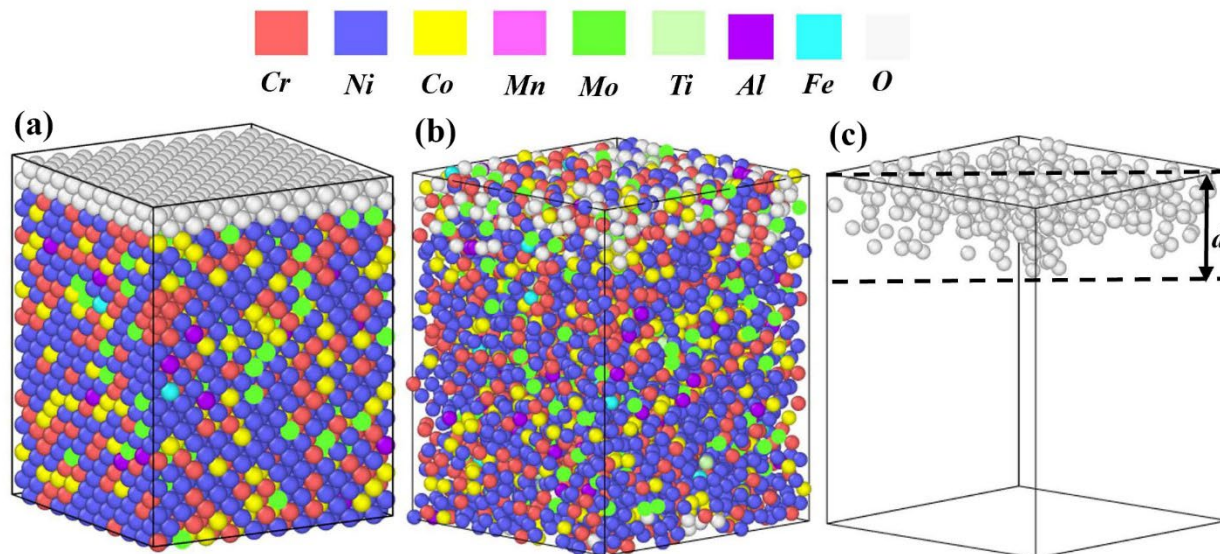


Figure 4. (a) Initial configuration of doubled layered oxygen atoms over the alloy surface. (b) Formation of oxide layer 100 ps after the initiation of simulation. (c) A schematic representing the oxygen atoms penetration depth.

### 2.1.3 Simulation Results

Simulation estimated tensile strength and oxygen penetration depths are summarized in Table 3. While IN617-M3 shows the lowest oxygen penetration (highest corrosion resistance), it also shows a low tensile strength relative to the IN617-M1 and IN617-M2 alloys. Therefore, the M1 alloy composition is the next best in terms of corrosion resistance, and it also possesses the highest strength. In short, compositional modification IN617-M1 exhibits superior strength and corrosion resistance despite having a lower cobalt (Co) content compared to IN617. IN617-M1 composition features a higher chromium content compared to IN617. Chromium is pivotal for forming a passive oxide layer (mainly chromium oxide) on the alloy surface, providing excellent corrosion resistance by acting as a barrier against further oxidation (Gusieva et al, 2015; Qiu et al. 2017; Roy et al., 2022). Additionally, chromium contributes to solid solution strengthening, enhancing the mechanical strength of the alloy.

Table 3. Average oxygen penetration depth and tensile strength for IN617 and its modifications. Only Co and Mn elemental compositions are noted for reference.

Alloy	Elemental wt.%		Avg. oxygen penetration depth (d) (Å)	Tensile strength (GPa)	
	Co	Mn		300 K	950 K
IN617	12.5	0.0	3.72	11.82	9.74
IN617-M1	2.5	5	3.35	12.33	10.03
IN617-M2	7.5	2.5	3.85	12.08	9.94
IN617-M3	2.5	10	3.08	11.67	9.74
IN617-M4	7.5	5	3.41	11.82	9.63
IN617-M5	10	2.5	3.70	11.66	9.63

In summary, modification IN617-M1's elemental composition, characterized by a higher chromium content along with balanced ratios of nickel, titanium, and aluminum, contributes to its superior strength and corrosion resistance. The presence of chromium facilitates the formation of a protective oxide layer on the alloy surface, while other elements contribute to strengthening mechanisms and microstructural refinement. Despite having a lower cobalt content compared to IN617, IN617-M1's overall composition enhances its mechanical performance and durability, making it the top choice for experimental validation.

## 2.2 Phase Diagram Calculations

All phase diagram calculations were carried out using Thermo-Calc 2024a software. The only databases available for this study are Fe/Steels (TCFE13) and High Entropy Alloys (TCHEA7); neither of them is tailored for nickel alloy compositions. Therefore, validating these available databases becomes crucial, which is performed by simulating the phase diagrams (Phase fraction versus temperature plots) for IN617 and comparing them with the experimental and modeling data in the literature. After the validation of the use of these databases for the Ni-based alloy systems (IN617), the validated database was used for the prediction of phase diagrams for other selected alloy compositions shown in Table 1. These modified alloy compositions were used for phase diagram calculations since they are new and lack any experimental data.

The TCHEA7 database failed to compute any results for IN617, while the TCFE13 (Fe/Steels database) was able to partially simulate the phase fraction versus temperature plots, as shown in Figure 5 below. It should be noted that some regions of the plot were not simulated, which emphasizes that the Fe/Steels database is not tailored for nickel alloys. The phase fraction versus temperature plot from Rai et al. (2017) is presented in Figure 6. Both the plots look almost identical, but the plot from our study revealed an additional phase, a  $\pi$  – phase, below 1000K.

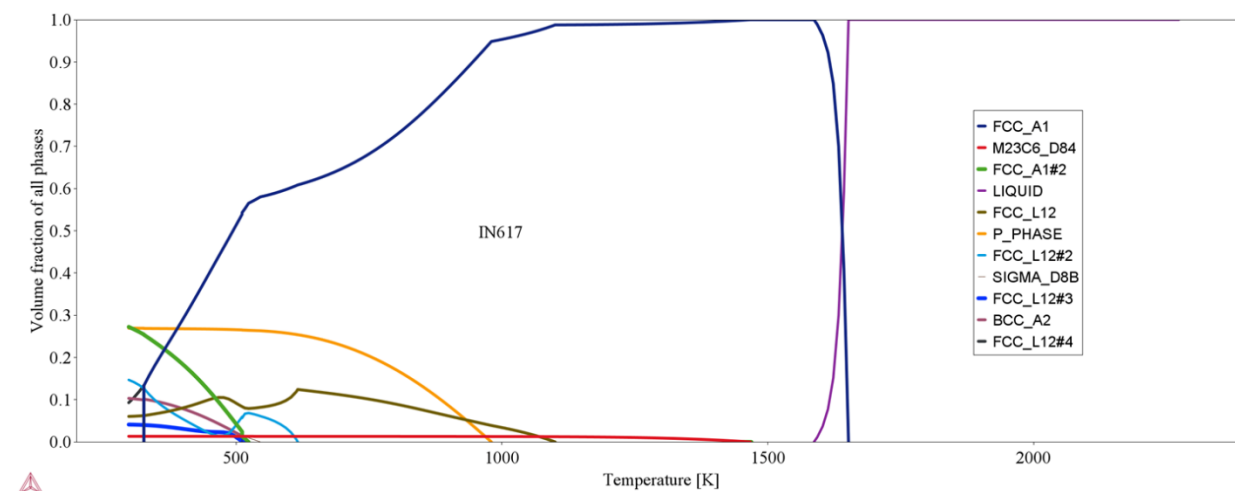


Figure 5. Phase fraction versus temperature plot for IN617 simulated using TCFE13 database and Thermo-Calc 2024a.

The formation of  $\pi$  – phases in IN617 alloy has been previously observed by Wang et al., (2023). An SEM image showing the  $\pi$  – phase, sourced from Wang et al. (20023), is presented in Figure 7 and validates the usage of Fe/Steels database for Nickel alloys.

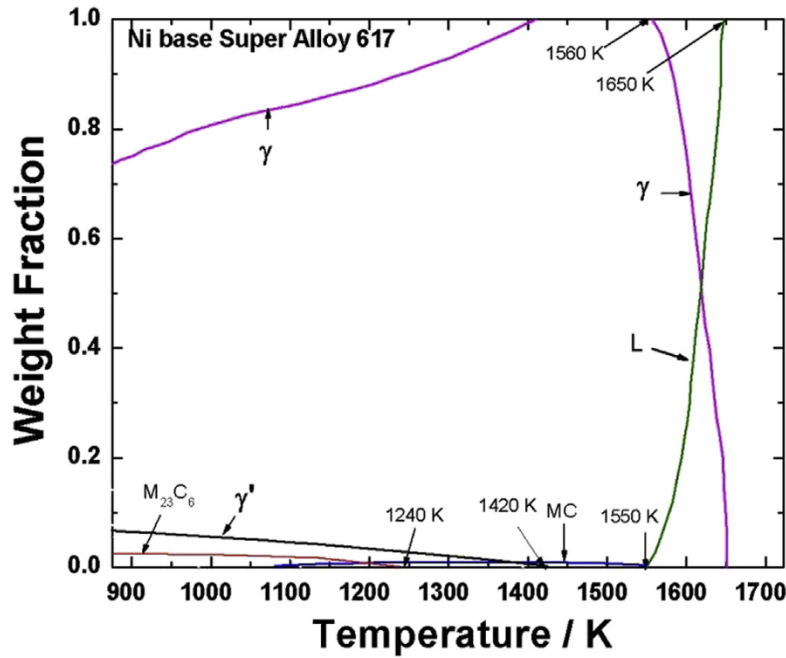


Figure 6. Phase fraction versus temperature plot obtained from Rai et al. (2017).

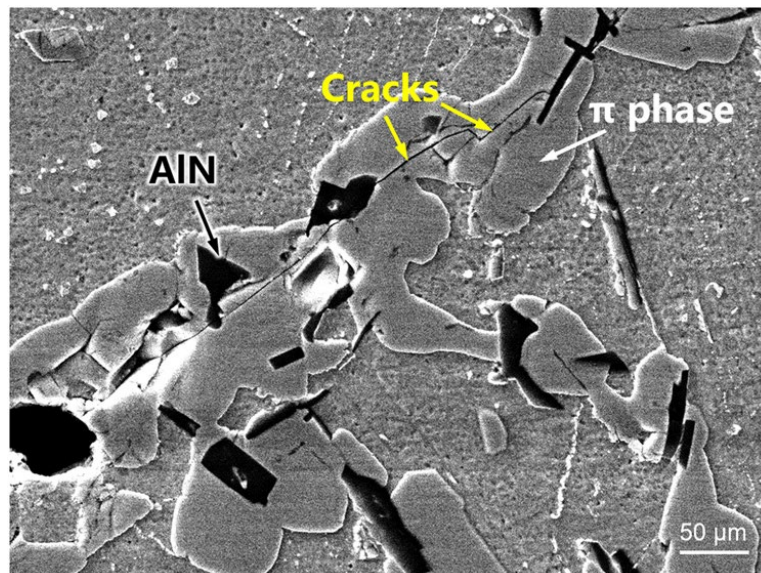


Figure 7. SEM image showing the presence of  $\pi$  phase in IN617 alloy. Image reproduced from Wang et al., (2023).

The phase fraction versus temperature data for IN617-M1 and IN617-M2 compositions are simulated using the TCFE13 database. These two alloy compositions were selected here since the Molecular Dynamics simulations performed on the modified alloy 617 compositions revealed the presence of high tensile strength values for IN617-M1 and IN617-M2 compositions. The corresponding plots are presented in Figure 8 and Figure 9, respectively. The TCFE13 database was not able to simulate the data throughout the temperature range (room

temperature to melting point) for the IN617-M1 alloy composition, while the same database was successful in predicting the full temperature range for the IN617-M2 composition. This could again be due to the fact that the Fe/Steels database does not contain data for, nor is it intended for use with Nickel alloys. The melting points of IN617-M1 and IN617-M2 are found to be 1267°C and 1280°C, respectively.

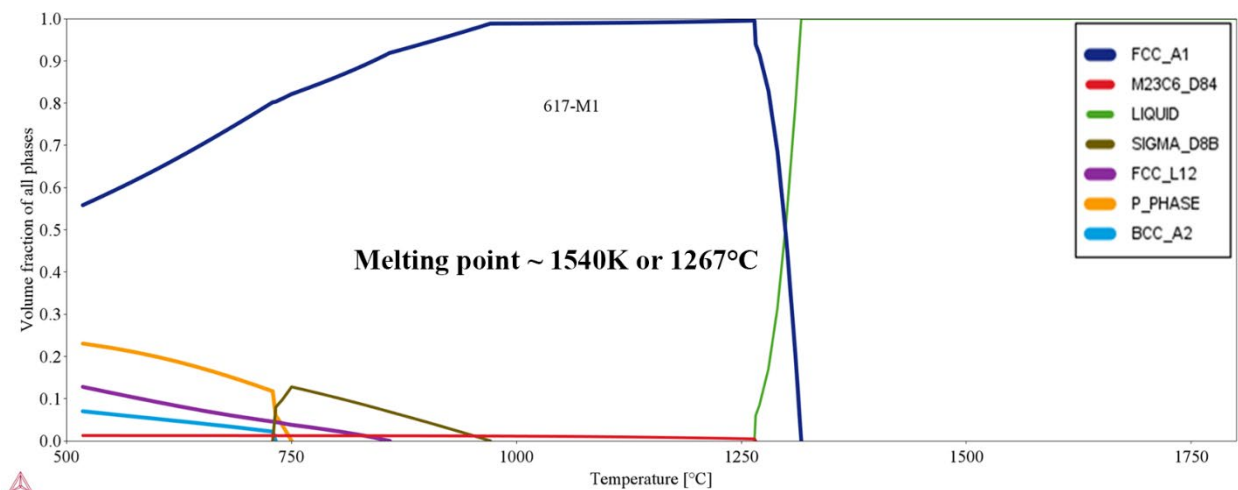


Figure 8. Phase fraction versus temperature plot for 617-M1 simulated using TCFE13 database and Thermo-Calc 2024a.

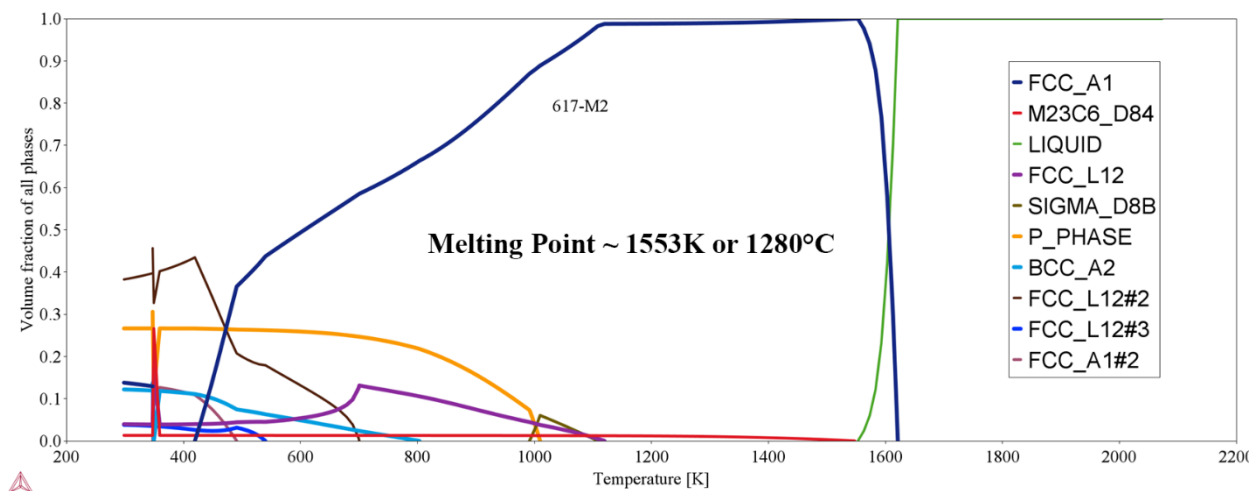


Figure 9. Phase fraction versus temperature plot for 617-M2 simulated using TCFE13 database and Thermo-Calc 2024a.

### 2.3 Experimental Validation of the MD Simulations

The IN617-M1 alloy recommended from the results of molecular dynamic modelling was produced using two different experimental techniques: traditional casting in an induction furnace and solid phase alloying through friction stir consolidation. For both approaches, wrought IN617 was turned into chips,  $4.5 \pm 0.7$ -mm-long by  $1.5 \pm 0.3$ -mm-wide, on a milling machine prior to mixing with the other elements to encourage a more homogenous product. Both methods are described in detail in this section.

### 2.3.1 Casting Using an Induction Furnace

Modifications of IN617 were made by adding pure elemental metals of Fe (99.99), Mn (99.95), Cr (99.99), Ni (99.995), Mo (99.95), Ti (99.995), and Al (99.999) to Inconel 617 to achieve a desired composition as informed by computer modeling. New compositions were weighed out on a Sartorius BCE224I-1S analytical balance to  $\pm 0.01$  g of the required amount for a 20-gram charge. The pure metals and bulk IN617 chips shown in Figure 10 were die pressed in a  $\frac{1}{2}$ " die set to 12000 lbs.; six pellets were pressed for a 20g charge, Figure 11.



Figure 10. 4N to 5N elemental purity pure elements, left. IN617 filaments and chips, middle and alumina crucible with pure elements and IN617 ready for casting.



Figure 11. Pure metal components and Inconel 617 chips pressed into pellets.

The pellets were then loaded in an alumina crucible with lid which was placed inside of a graphite crucible. The graphite crucible was then loaded into a 25KW MTI Corp. EQ-SP-25A Induction Heater with a custom-made coil with 7 windings of  $\frac{3}{8}$ " copper tubing with an inner diameter of  $\sim 2.75$ " and height of  $\sim 4$ ". The coil also contained insulation and an inert gas line, as shown in Figure 12. Argon was flowed prior to and during the melting procedure to reduce oxidation, and a type R thermocouple was inserted through top of the crucible setup to monitor, adjust, and record temperatures. An initial temperature evaluation study was performed with two thermocouples, it showed the temperature varied by  $40$ - $80^\circ\text{C}$ , the internal crucible being higher as it had better contact with the bottom of the crucible. Graphite was used as a susceptor to reach temperatures exceeding  $1700^\circ\text{C}$  which were held for 30 minutes to alloy the metal components, as shown in Figure 12. The temperature profile collected from a thermal couple placed on the graphite crucible is shown in Figure 13. The temperature was held for 30 minutes to allow the heat to soak into the inner alumina crucible and fully melt the charge inside. This

holding time and target temperature were determined during previous testing. The furnace was allowed to cool to room temperature, and the ingot was extracted from the alumina crucible, Figure 14. The ingot was sectioned, mounted, and polished to 1  $\mu\text{m}$  for further examination.



Figure 12. MTI 25 kW Induction furnace with induction coil, left, coil, insulation, and internal crucible setup used for alloying new metal compositions, right.

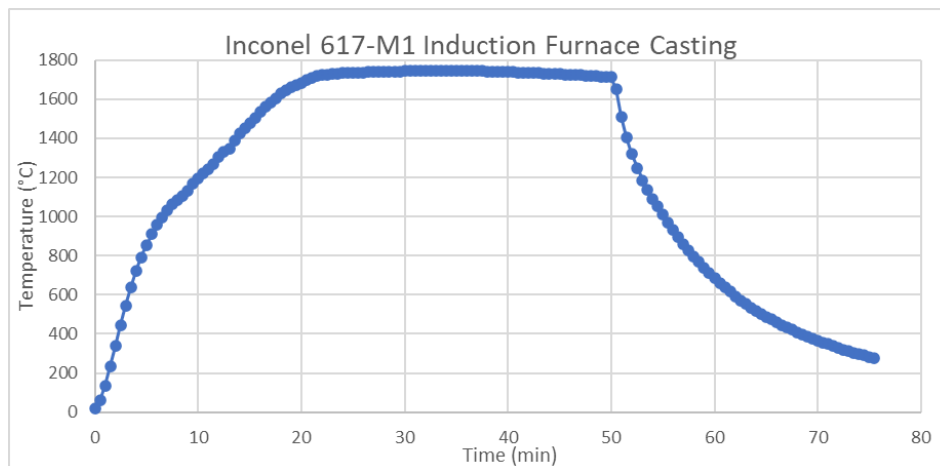


Figure 13. Temperature profile used to melt Inconel 617-M1.

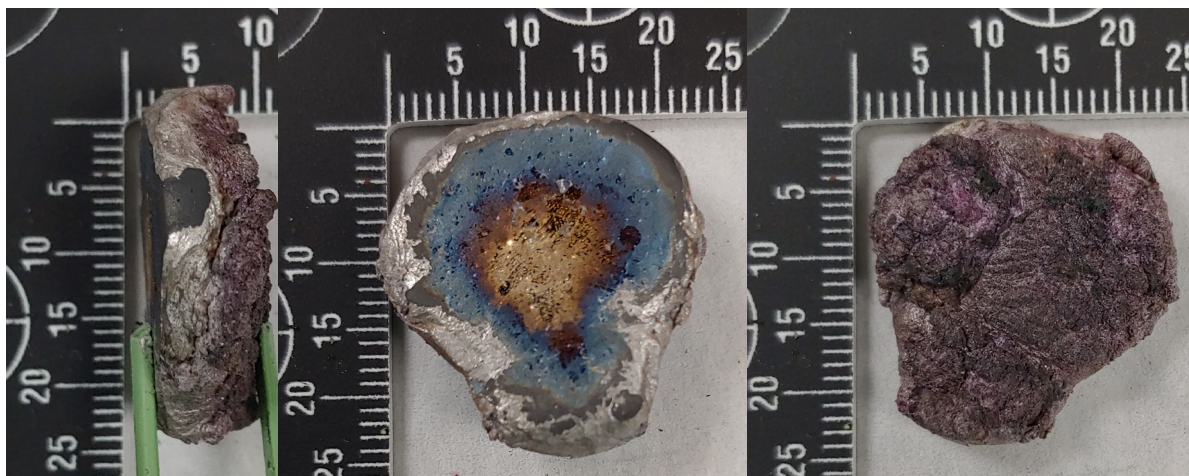


Figure 14. IN617-M1 ingot formed, max temperature of 1740°C, from left to right -Side, Bottom, and Top of ingot.

The induction melter was able to make the alloy and could be used for further studies. However, other methods may be more suitable to achieve the grain structure for ideal mechanical properties testing such the ability to pour and cast to shape, or use of an arc melter for fast cooling and rapid turn-around.

### 2.3.2 Friction Consolidation and Solid Phase Alloying

IN617 chips were fabricated by machining Inconel 617 sheet metal using a milling machine. The IN617 chips were then mixed with 4N and 5N pure metals described previously in the quantities given in Table 4. Approximately 30 g of mixed metal chips were used for each consolidation experiment, as shown in Figure 15.

Table 4. Metal masses used for friction consolidation and solid phase alloying runs.

Run Number	Cr g	Ni g	Mn g	Mo g	Ti g	Al g	Fe g	IN617 g	Total, g
Run 1	6.6876	12.8415	1.5006	2.2792	0.4132	0.2878	0.2171	5.9796	30.2066
Run 2	6.6909	12.8774	1.5186	2.2853	0.3918	0.2925	0.2200	5.9766	29.9005



Figure 15. A mixture of Inconel 617 chips and pure metal alloying additions.

The friction consolidation and solid phase alloying experiments were performed using a Transformational Technology, Inc. LS2-2.5 friction stir welding (FSW) machine, with a tungsten-rhenium (W-Re) tool coupled with a tool holder, as shown in Figure 16.



Figure 16. Friction consolidation and solid phase alloying setup.

Critical process variables during friction consolidation experiments include the loading force, rotation rate, and processing time. The tool/chip interface temperature is measured and monitored during friction consolidation and is a key parameter in determining the extent of consolidation. Temperature is directly influenced by the loading force and rotation rate during friction consolidation. The critical parameters of the two friction consolidation and solid phase alloying runs performed using IN617-M1 chips are listed in Table 5. A loading force of 65 kN was selected for both runs with rotation rates of 100-35 RPM for Run #1 and 100-50 RPM in Run #2, enabling us to maintain a consistent tool/chip interface temperature of  $\sim 900^{\circ}\text{C}$ .

Table 5. Critical parameters for friction consolidation of 617M1 alloy chips.

Run #	Weld #	Tool	Loading (kN)	Rotation rate (RPM)	Temperature ( $^{\circ}\text{C}$ )	Processing time (min)
1	2024-07-23-#000	W-Re	65	100 to 35	Up to 900	8
2	2024-07-24-#000	W-Re	65	100 to 50	Up to 900	3 min to abort

Machine data, including tool position (Z position), loading force (Z-axis force), temperature, rotation rate, spindle torque, and spindle power are plotted in Figure 17. A rapid reduction in rotation rate during the friction consolidation during Run #2 caused a sudden increase in torque that reached the maximum torque of the FSW instrument of 700 Nm, causing the run to abort. As a result of the over torque the W-Re tool got stuck to the chips container and was recovered using electrical discharge machining (EDM) wire cutter.

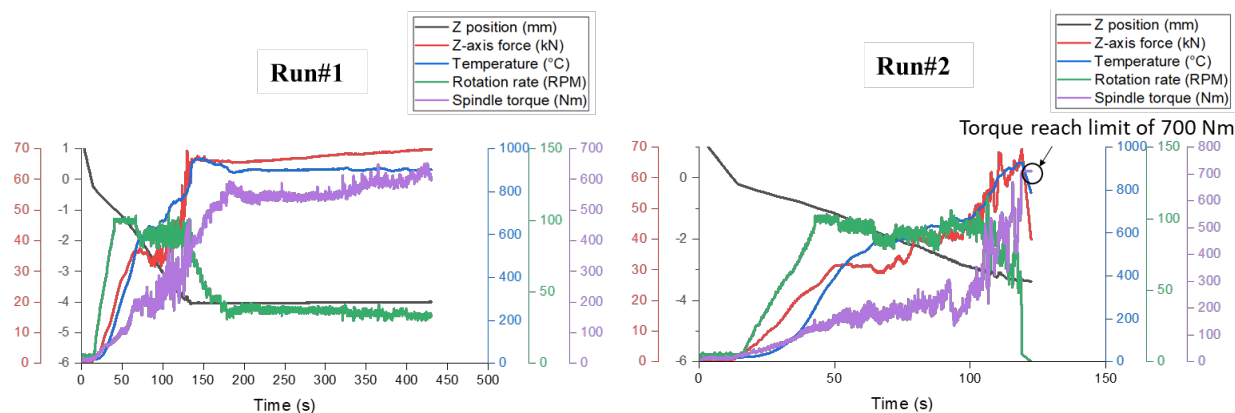


Figure 17. Machine data of tool position (Z position), loading force (Z-axis force), tool/chip interface temperature, rotation rate and spindle torque for Run #1 and 2.

Side and top view images of the consolidated and alloyed chips are shown in Figure 18 for both test runs. Visual inspection of the consolidated and alloyed material suggests that a loading force of 65 kN was sufficient to obtain a fully consolidation material. This value was selected based on our previous experience with similar metal systems. Parameters that are typically adjusted to improve consolidation and alloying include the loading force/rotational speed combination and hence temperature and process durations.



Figure 18. Top- and bottom view of consolidated and alloyed chips for Run #1 and #2.

## 2.4 Characterization Results and Discussion

In this section, the characterization of the alloys produced from casting, and friction stir consolidation and solid phase alloying are presented. Vickers hardness was determined as an experimentally rapid method of obtaining information that can be correlated to yield strength which was used by the MD simulations to assess the different alloy modifications. SEM-EDS was also performed on each of the samples giving us insight into the grain boundaries, grain sizes and chemical composition. XRD was also performed on the casting sample to verify phases present.

### 2.4.1 Characterization Methods

In preparation for SEM-EDS and Vickers hardness testing, the as-cast IN617-M1 and the FSA IN617-M1 samples were mounted in epoxy and prepared metallographically with grinding and polishing. All samples were given a final polish using 1  $\mu\text{m}$  diamond polishing paste and a colloidal silica (0.05  $\mu\text{m}$ ) polishing suspension. Once the final polishing was completed, samples were examined using Olympus DSX510 metallurgical microscope.

A JEOL 7600 SEM operating at 20kV was used to capture backscattered imaging and compositional analysis of the as-cast IN617-M1 alloy using X-ray energy dispersive spectroscopy (XEDS, Oxford Instruments). Imaging and compositional analysis of the IN617-M1 friction stir consolidation alloy was carried out using a ThermoFisher Apreo™ 2 instrument.

Vickers microhardness measurements were performed using a Sun-Tec (model CM-802 AT) microhardness tester, operated with the ARS20 software for automated measurements. A load force of 300 grams-force was applied for a duration of 10 seconds for each indentation. A 2 x 2 array of indentations was performed on three regions of the IN617-M1 cast alloy (potentially matrix), each indentation was separated by 0.5 mm. SEM-EDS analysis confirmed the target composition of the sample was approximately equivalent to the targeted M1 formulation. The friction alloyed sample (IN617-M1 Run#1) was analyzed using a 2 x 10 array of indentations performed on two regions consisting of four lines indicated as L-1, L-2, L-3, and L-4 in Figure 6-4 (a). The FSA IN617-M1 Run#2 sample was analyzed using a 3x3 array of indentations performed on a region which was observed to have less pores.

Calibration checks for the hardness measurements were conducted using Sun-Tec calibration standards 297HV0.3 to verify that the instrument was in calibration. These checks confirmed that the hardness values measured were within  $\pm 2\%$  of the calibration standard, ensuring the accuracy of the measurements.

Powder XRD using a D6 Phaser (Bruker Inc.) diffractometer was used to collect the XRD patterns of Inconel 617 and our modified IN617-M1 sample. Both samples were mounted in epoxy, resulting in a high background, especially at low angles. The D6 Phaser is equipped with a Theta/Theta Goniometer with a radius of 166.5 mm, a Cu  $K_{\alpha}$  radiation, and a 1.2 kW X-ray power generator. Prior to collecting the XRD patterns, samples were aligned, and the NIST SRM 640g internal standard was used for precision sample displacement correction. All the XRD patterns were collected using  $0.01^{\circ}$   $2\theta$  step size and 0.32 s time per step over  $10-120^{\circ}$   $2\theta$  range. Each scan took  $\sim 1$  h to complete.

#### **2.4.2 Characterization Results of IN617-M1 Cast Alloy**

The results obtained from the mechanical testing and chemical analysis of the IN617-M1 cast alloy sample are discussed in the sections below.

### 2.4.3 Optical Imaging and Vickers Hardness IN617-M1 Cast Alloy

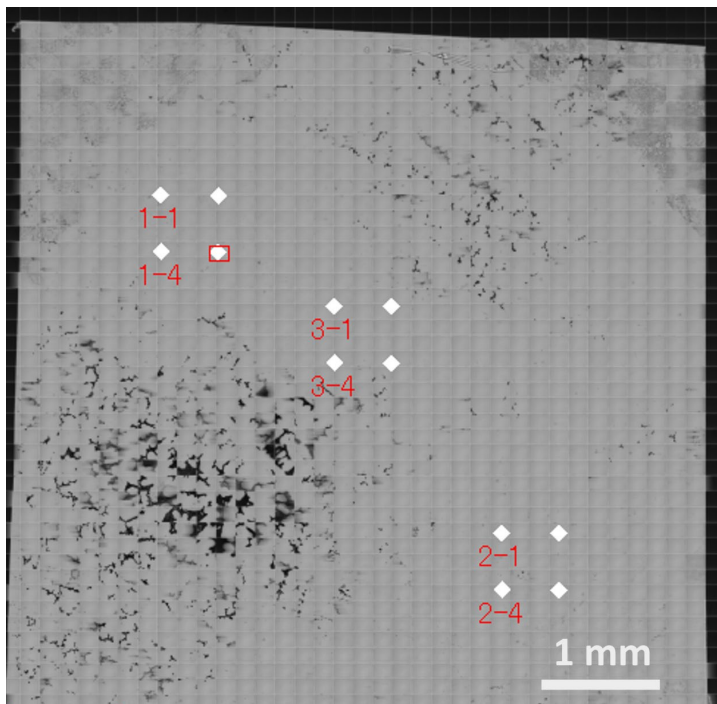


Figure 19. Optical micrographs of as-cast IN617-M1 sample with indents for Vickers hardness measurement.

Figure 19 presents the optical micrographs of as-cast IN617-M1 sample. Three regions (potentially matrix) were selected and a 2x2 array of indentations was performed on the selected regions to determine the hardness. The as-cast IN617-M1 sample had regions with porosity while other regions were fully dense. The Vickers hardness data of the as-cast IN617-M1 sample is given in Table 6. The indentation regions are indicated in Figure 19.

The average hardness values obtained from the three arrays of indents for the casting sample are given in Table 6, all three averages are self-consistent with each other, with an average of  $194.89 \pm 9.71$  HV.

Table 6. Vickers hardness values for the as-cast IN617-M1 alloy for the indentation regions marked in Figure 19.

Indentation Region	Vickers Hardness, HV	Average Vickers Hardness, HV	Average of all the Readings, HV
1	199.49	199.76 ± 11.51	194.35 ± 9.71
	212.52		
	181.48		
	205.53		
2	193.47	197.04 ± 2.08	
	198.51		
	197.78		

Indentation Region	Vickers Hardness, HV	Average Vickers Hardness, HV	Average of all the Readings, HV
3	198.38	187.88 ± 8.27	
	185.5		
	201.97		
	181.59		
	182.45		

#### 2.4.4 XRD IN617-M1 Cast Alloy

The X-ray diffraction patterns of IN617 and our Mn rich, IN617-M1, modified alloy are shown in Figure 20. Both alloys show similar solid-solution phases (fcc phases), with a peak shift to the low-angle in the IN617-M1 suggesting a larger lattice parameter than that of the unmodified IN617 sample. The increase in the lattice parameter may reflect the incorporation of Mn into the IN617 matrix while the Peak broadening is likely due to a smaller crystallite size and higher lattice strain in the sample compared to the unmodified IN617 material.

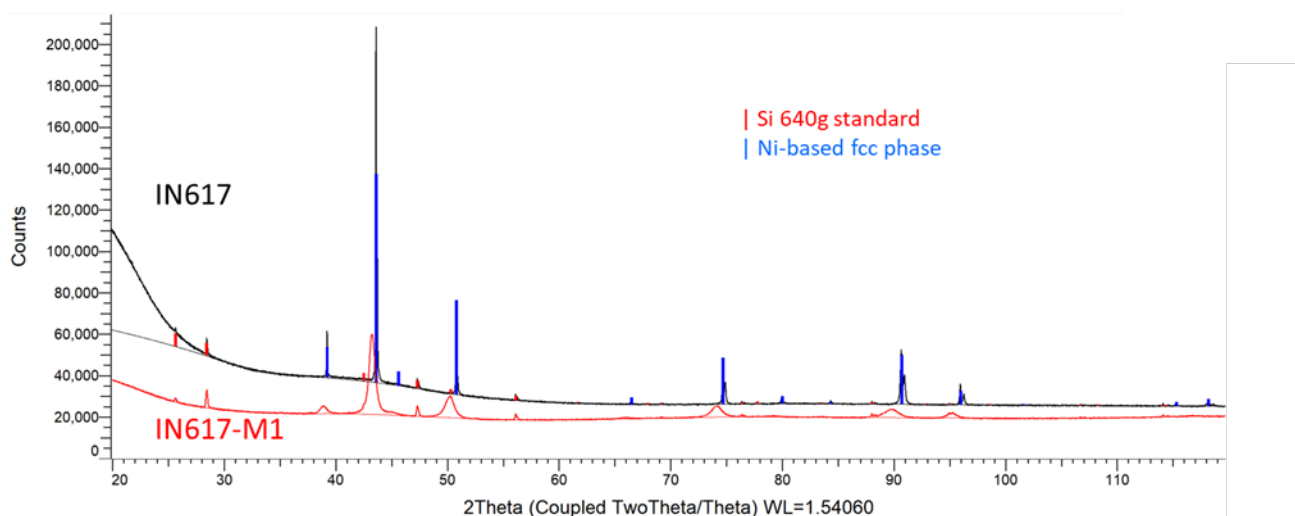


Figure 20. Comparison of IN617-Co 12.5 wt% and the modified IN617-M1-Co 2.5 wt% alloy sample from casting at  $\sim 1700^{\circ}\text{C}$  using and induction furnace. Peaks correspond to the Si standard (NIST SRM 640g) and fcc phase are denoted by red and blue tick marks, respectively.

#### 2.4.5 Compositional Analysis IN617-M1 Cast Alloy

Figure 21 presents the XEDS compositional mapping of the backscattered electron (BSE) micrographs of the as-cast IN617-M1 sample. Six regions/points were identified from the sample and detailed analysis were performed. The primary purpose was to determine whether the composition of the matrix hit the composition close to M1 target (Co substitution by Mn). The un-melted material identified as Block 1 was observed to be Ti enriched which has a higher melting point than the base alloy IN617-M1. The precipitates (ppt) decorated within the grain boundary (GB) was observed to be Cr, Mo and Mn enriched. Detailed compositional analysis of the identified region is present in Table 7. From this table, the matrix composition is found to be very close to the IN617-M1 composition.

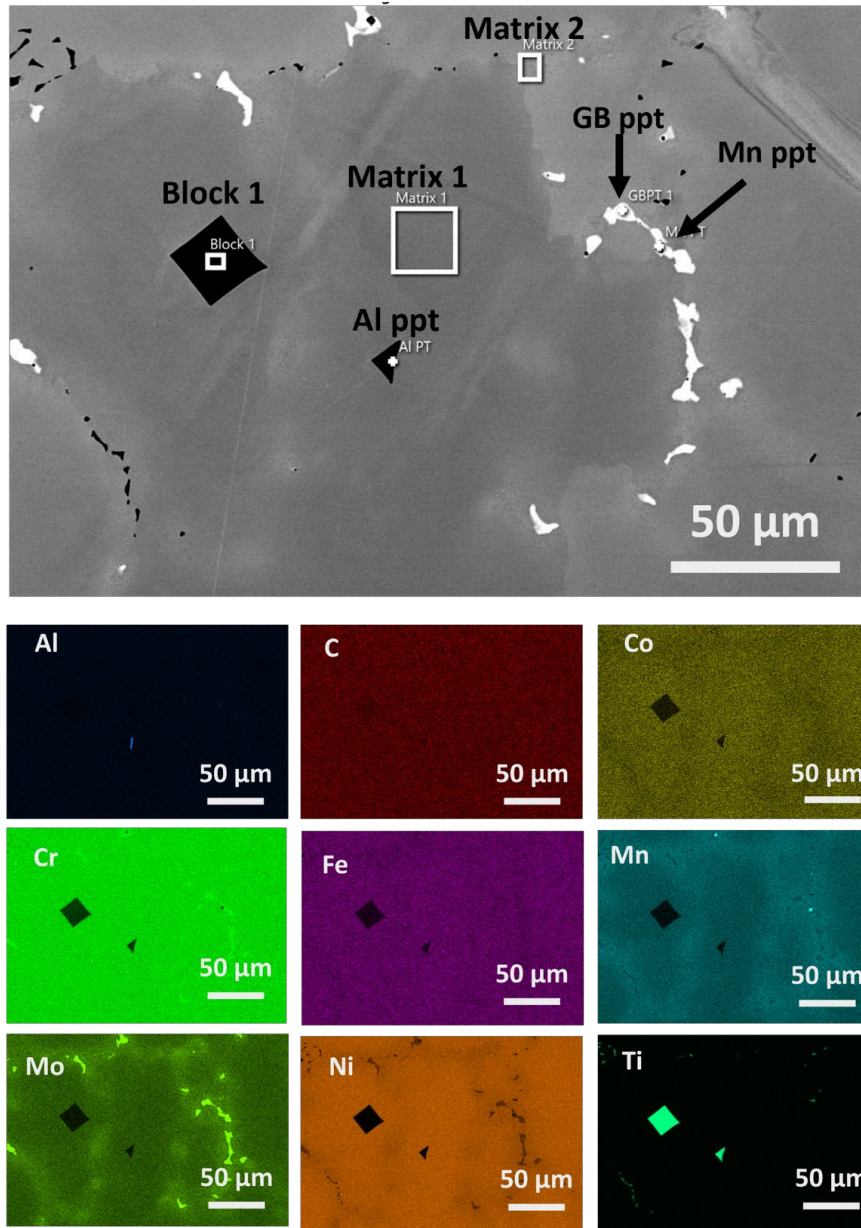


Figure 21. XEDS compositional mapping of the backscattered electron micrographs of IN617-M1 cast alloy.

Table 7. Elemental composition of regions highlighted in Figure 21 IN617-M1 composition included for comparison.

Location	C	Al	Ti	Cr	Mn	Fe	Co	Ni	Se	Mo	Total
IN617-M1	0.06	1.2	0.3	26.6	5	0.9	2.5	53.6	-	9.5	99.66
Map Sum 1	0.06	0.71	0.80	27.28	4.61	1.65	2.28	52.26	0.00	10.35	100.00
Matrix 1	0.06	0.67	0.07 <sup>(a)</sup>	27.31	3.69	1.83	2.51	55.98	0.00	7.87	100.00
Block 1	0.06	0.00	87.13	11.37	0.12 <sup>(a)</sup>	0.00	0.00	0.63	0.00	0.69	100.00
Matrix 2	0.06	0.65	0.06 <sup>(a)</sup>	28.33	5.85	1.38	2.02	48.01	0.00	13.64	100.00
Mn PT	10.1	0.42	0.00	5.87	31.09	0.33	0.27	5.99	26.16	19.78	100.00
GBPT 1	10.07	0.17	0.00	29.51	3.24	0.95	1.57	25.10	0.00	29.39	100.00
Al PT	0.06	22.78	62.92	9.97	0.20 <sup>(a)</sup>	0.16 <sup>(a)</sup>	0.15 <sup>(a)</sup>	2.96	0.00	0.79	100.00

(a) Trace elements below confidence threshold

#### 2.4.6 IN617-M1 Friction Stir Alloying

The results obtained from the mechanical testing and chemical analysis of the IN617-M1 friction stir alloy sample are discussed in the sections below.

#### 2.4.7 Optical Imaging and Hardness

Figure 22(a) presents the optical micrograph of the FSA IN617-M1 Run#1 sample along with the indents performed and Figure 22(b) presents the Vickers hardness as a function of datapoints. Four lines identified as L-1, L-2, L-3, and L-4 consisting of 10 indentations were performed on the sample to determine the variation in hardness parallel to the flat surface (top) of the sample which is assumed to be the starting point of the FSA fabrication process. In general, this FSA IN617-M1 Run#1 was observed to show higher hardness as compared to the as-cast IN617-M1 sample.

Table 8. Summary of Vickers hardness values measured for both casting and friction stir alloying.

Sample Type	Array of Indents	Indented Region	Vickers Hardness, HV Load 300 gf, Dwell Time 10s, Spacing 0.5 mm	Average Hardness, HV
As-Cast IN617-M1	2 x 2	1	199.76 ± 11.51	194.35 ± 9.71
		2	197.04 ± 2.08	
		3	187.88 ± 8.27	

Sample Type	Array of Indents	Indented Region	Vickers Hardness, HV Load 300 gf, Dwell Time 10s, Spacing 0.5 mm	Average Hardness, HV
FSA IN617-M1 Run #1	2 x 10	1	348.18 ± 36.65	346.68 ± 45.64
		2	345.17 ± 53.10	
FSA IN617-M1 Run #2	3 x 3	1	180.25 ± 18.77 <sup>(a)</sup>	180.25 ± 18.77

(a) One indent result was excluded from the average because it fell on the pores.

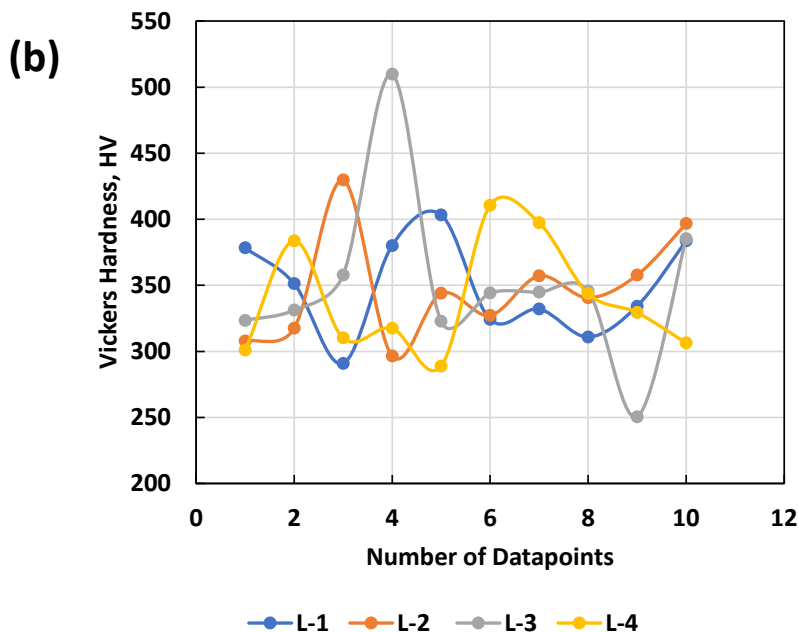
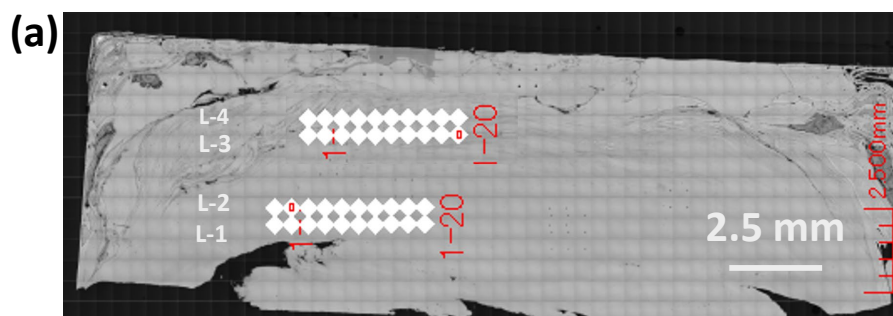


Figure 22. Optical micrographs and Vickers hardness FSA IN617-M1 Run#1 sample, (a) OM with indents and, (b) Vickers hardness as a function of data points

### 2.4.8 Microstructural Analysis of FSA IN617-M1 Run#1

Figure 23(a-c) presents the BSE micrograph of FSA IN617-M1 Run#1 sample. The lower magnification images in Figure(a-b) shows variation in image contrast that represents inhomogeneity in the alloy. However, a higher magnification image in Figure 23(c) shows formation of small equiaxed grains in the alloys with significant amount of porosity. The grain

size was measured using ImageJ and it was observed to be  $1.67 \pm 0.39 \mu\text{m}$ . The higher hardness observed in the FSA IN617-M1 Run#1 sample could potentially be attributed to this small grain size. Figure 23 (d) is an inverse pole figure image from the same alloys that shows the distribution of FCC grains. From these results, it can be inferred that the FSA process is able to form alloys with uniform grain sizes, but further process optimization is need for macroscopic chemical homogeneity.

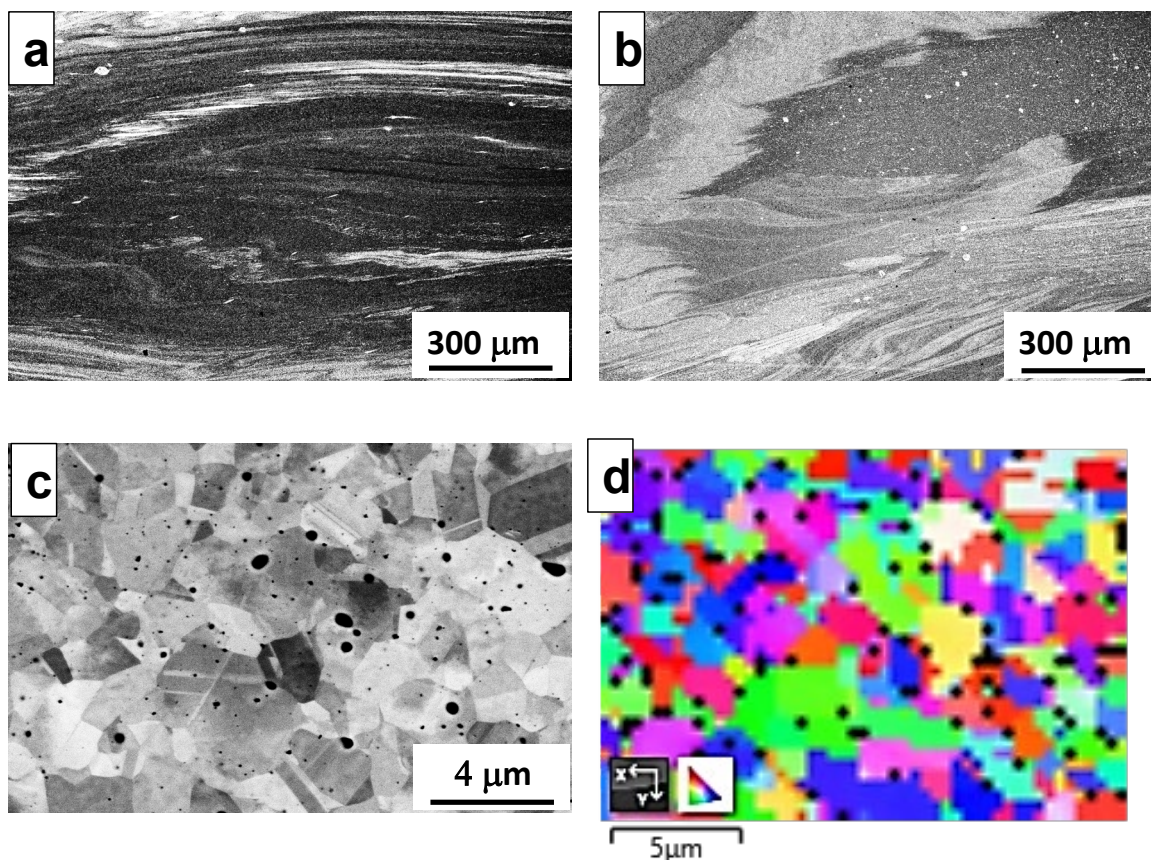


Figure 23. (a-c) show BSE micrograph of FSA IN617-M1 Run#1 sample, (d) shows the inverse pole figure of this alloy.

#### 2.4.9 Compositional Analysis IN617-M1 Run #1

A localized area in the FSA IN617-M1 Run #1 sample was analyzed for chemical compositions, as presented in Figure 24. The compositional evaluation was carried to confirm the presence of all intended elements for the IN617-M1 chemistry. The observed uniformity of composition across this smaller region indicates that further process parameter optimization is required for fabricating dense homogeneous products. This localized region also has composition close to IN617-M1 (Table 9). The presence of Si at pores is mostly due to the residual Si used for polishing the samples.

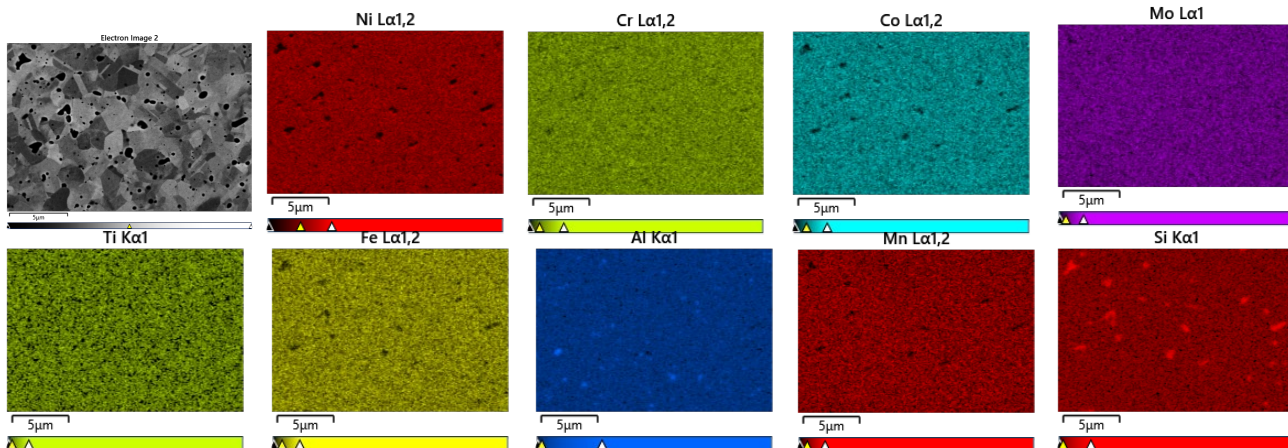


Figure 24. XEDS compositional mapping of the backscattered electron micrographs of IN617-M1 Run#1 FSA sample.

Table 9. The chemical composition of the IN617-M1 Run#1 FSA sample corresponding to Figure 24.

Ni	Cr	Mn	Fe	Co	O	Mo	Al	Si	Ti
54.14	33.51	4.23	3.22	2.67	1.44	0.42	0.25	0.1	0.03

#### 2.4.10 Microstructural Analysis of FSA IN617-M1 Run#2

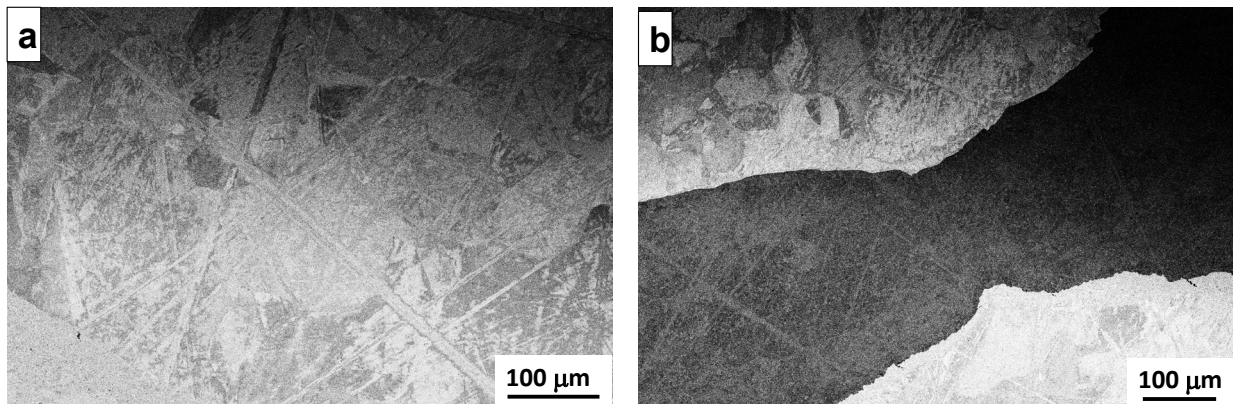


Figure 25. (a-b) shows the BSE images of FSA IN617-M1 Run#2 sample that shows the chemical inhomogeneity through the variation in image contrast.

The BSE micrograph of FSA IN617-M1 Run#2 sample is presented in Figure 25 (a-b). During processing of this Run#2 sample, a rapid reduction in rotation rate caused a sudden increase in torque that reached the maximum torque of the FSW instrument of 700 Nm, causing the run to abort in less than 3 mins. Significant macroscopic chemical inhomogeneity was observed in this sample as evident in the XEDS compositional mapping presented in Figure 26 (a-b). Moreover, it did not get enough time for recrystallization as the process was aborted within 3 mins. As such, the measurement of grain size was not possible, contrasty to that in Run#1. The lower hardness in FSA IN617-M1 Run#2 sample could also be attributed to this significant chemical

inhomogeneity. The results from Run#1 and #2 suggests that the process parameter need to be optimized further for obtaining materials with less porosity and chemical homogeneity.

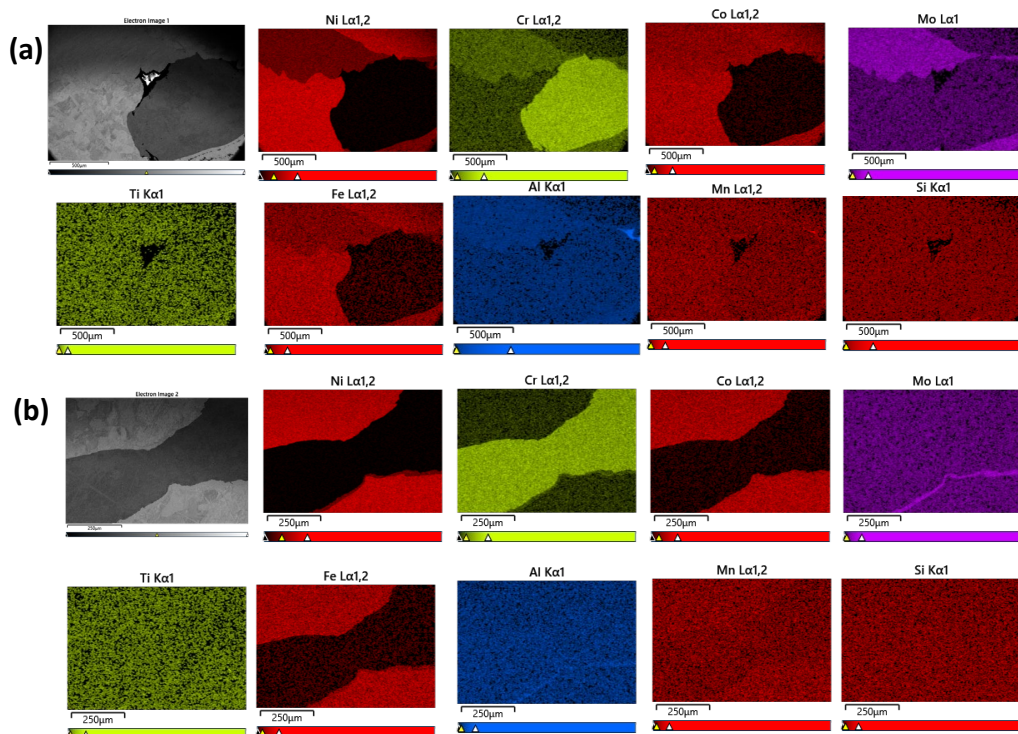


Figure 26. (a-b) XEDS compositional mapping of the backscattered electron micrographs of FSA IN617-M1 Run #2 sample. The chemical inhomogeneity is pronounced in this sample.

## 2.5 MD Performance Conclusion

Krishna et al (2010) reported the Vickers hardness of solution annealed IN617 to be  $186.6 \pm 5$  HV when measured with a load of 20 kgf. This value is comparable to the as-cast IN617-M1 hardness value of  $194.35 \pm 9.7$  HV obtained in this study. Table 10 summarizes the grain size in microns and the Vickers hardness values (HV) of the MD informed IN617-M1 formulation results for both the casting alloy and the FSA samples along with unmodified IN617. The FSA IN617-M1 Run#2 sample was found to be highly heterogenous, most likely due to the short run time resulting from the instrument aborting due to exceeding the maximum allowable torque, thus a grain size could not be determined.

Table 10. Comparison of MD performance compared to experimental data.

Alloy Studied	Grain Size, $\mu\text{m}$	Hardness, HV	Ref
As-cast IN617	10.2	$230.7 \pm 6.8$	van Rooyen et al. (2024)
Solution Annealed IN617	120	$186.6 \pm 5$	Krishna et al. (2010)
FSA IN617	1.35	$356.5 \pm 15.8$	van Rooyen et al. (2024)
As-cast IN617-M1	$\sim 800$	$194.35 \pm 9.71$	This work
FSA IN617-M1 Run#1	$1.67 \pm 0.39$	$346.68 \pm 45.64$	This work
FSA IN617-M1 Run#2	-	$180.25 \pm 18.77$	This work

IN617-M1 shows considerable promise as a material, particularly when subjected to advanced processing methods like friction stir alloying (FSA) due to the grain refinement as an additional strengthening mechanism. In the as-cast condition, IN617 exhibits a hardness of  $230.7 \pm 6.8$  HV with a grain size of  $10.2 \mu\text{m}$ , while as-cast IN617-M1 has a lower hardness of  $194 \pm 9.71$  HV, accompanied by a much larger grain size of  $800 \mu\text{m}$ . This reduction in hardness for M1 is likely due to the significant difference in grain size, as smaller grains typically provide more barriers to dislocation movement, resulting in higher hardness. The larger grain size in IN617-M1 naturally leads to lower hardness, but this doesn't necessarily indicate poor performance, especially considering the potential for grain refinement through processing.

When subjected to FSA, both IN617 and IN617-M1 show significant improvements in hardness due to grain refinement. FSA IN617 achieves a hardness of  $356.49 \pm 15.8$  HV with a grain size of  $1.35 \mu\text{m}$ , while FSA IN617-M1 reaches a hardness of  $346 \pm 45$  HV with a slightly larger grain size of  $1.67 \mu\text{m}$ . The minimal difference in hardness between the two alloys after FSA processing suggests that M1 can achieve nearly equivalent mechanical performance to IN617 when its grain structure is refined. This is consistent with molecular dynamics (MD) predictions, where M1 exhibited a slightly higher tensile strength ( $12.33$  GPa) compared to IN617 ( $11.82$  GPa), indicating its potential for superior mechanical properties.

In summary, while as-cast IN617-M1 exhibits lower hardness due to its coarser grain structure, the alloy shows great potential when processed to refine its microstructure. The close match in hardness between FSA IN617 and FSA IN617-M1, along with the MD predictions of higher tensile strength for M1, suggests that M1 is as promising as IN617 for applications requiring high strength, particularly when processing techniques like FSA are employed to optimize its grain structure.

### 3.0 New Alloy Development Using Multi Objective Bayesian Optimization

The objective of the new alloy development is to develop new alloys having high hardness and yield strength without critical minerals (i.e., nickel and cobalt using a multi objective Bayesian optimization (MOBO) technique). The high entropy alloy (HEA) system within which new compositions were developed is Fe-Cr-Cu-Al-Nb-Ta-Ti-V-Zr-Mo-W-Mn. Both the objectives are optimized by learning the Pareto front (i.e., learning a set of non-dominated solutions where each point on the Pareto front is a compromise between the multi objectives namely hardness and yield strength).

Most of the Machine Learning (ML) research in developing HEA have been focused on predicting a single physical property like hardness, yield strength or young modulus (Khakurel et al, 2021; Taufique et al., 2024; Wen et al., 2019). There has been a gradual shift to leverage ML and statistical methods to optimize two or more physical properties for an HEA system using methods like Generative Adversarial Networks (GAN), multi objective optimization techniques like non-dominate sorting genetic algorithm (NSGA) and Bayesian optimization (Li et al., 2024; Solomon et al., 2018; Shi et al., 2023). In this study, MOBO was used to develop new material compositions without the critical minerals—nickel and cobalt with maximum yield strength and hardness. Two Neural Network models were developed to predict Yield Strength and Hardness using two separate datasets available on Yield Strength and Hardness (Taufique et al., 2024) and these models were used to predict the hardness and yield strength of new compositions developed through multi-objective Bayesian optimization. From all the new compositions developed, optimal solutions were learned from the Pareto front.

#### 3.1 Design Strategy

The design strategy used to develop new alloys using MOBO is depicted in the Figure 27. A database of alloys was curated which had both their hardness and yield strength data measured at room temperature. This data was used to train a Gaussian Process Model (i.e., a surrogate model to model the unknown objective function for both hardness and yield strength). Once a surrogate model is established to model the objective function from the curated data, Acquisition function uses the surrogate model to establish the next point or set of points in the search space within the bounds and constraints set.

The hardness and yield strength models developed separately are used to predict hardness and yield strength for these new candidate/ candidates. A separate hardness and yield strength database is used to develop these separate models for hardness and yield strength. The newly generated candidates and their predicted hardness and yield strength values are added back to original curated dataset and the whole cyclic process of approximating the unknown objective function and predicting next set of candidate/ candidates using acquisition function and their hardness and yield strength value is repeated for several iterations. At the end of scheduled number of iterations, the hardness and yield strength of all curated alloys and new compositions are plotted together to extract the Pareto front. The solutions obtained in the Pareto front are to be analyzed using Molecular dynamics. The aim being to fabricate and test the hardness and yield strength of those solutions on Pareto Front (non-dominated solutions) whose performance can be validated using Molecular dynamics.

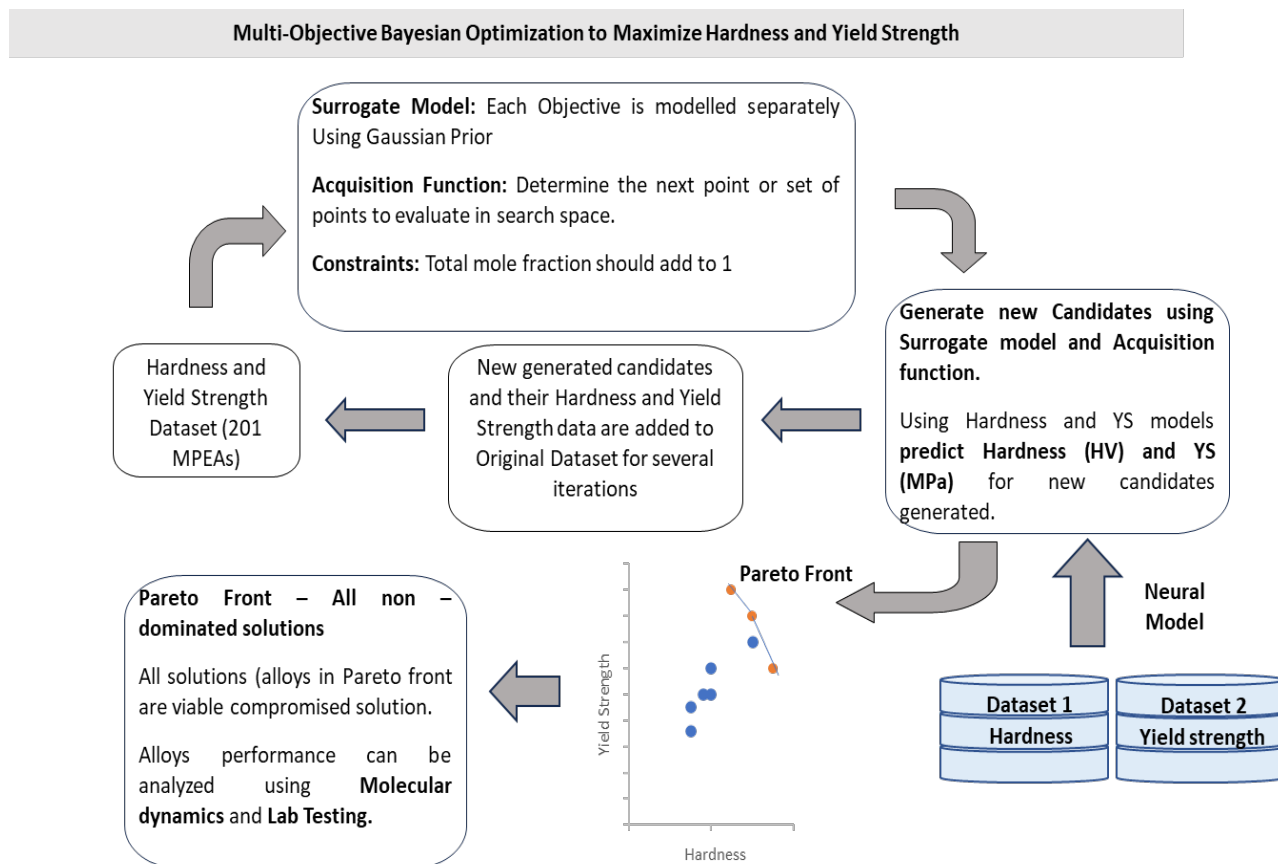


Figure 27. Multi objective Bayesian optimization framework.

### 3.2 Hardness and Yield Strength Model

Data on Yield Strength (MPa) and Hardness (HV) used are previously collected data from existing literature (Taufique et al., 2024; Gorsse et al., 2018; Couzinié et al., 2018). The dataset for yield strength model contains yield strength data on 160 multi-principal metal alloys (MPEAs) and HEAs curated from literature is included in Appendix A.1 (Taufique et al., 2024). The dataset for hardness model contains hardness data on 243 MPEAs and HEAs curated from literature is included in Appendix A.2 (Taufique et al., 2024).

Neural Models were used to train two separate models to predict yield strength and hardness respectively using the curated yield strength and hardness data from their respective datasets (Appendices A.1 and A.2) and 14 computed features related to MPEAs. These features have been found to have an effect on the mechanical properties of MPEAs (Roy et al., 2022; Khakurel et al., 2021). The data on elemental values for features like Valence Electron Concentration (VEC), Pauling and Allen electronegativity, enthalpy, atomic radii, lattice constants were gathered from various domain-specific sources (Takeuchi and Inoue, 2005). These 14 features were computed for all the Alloys using Python scripts; details on the 14 features computed are available in Table 11.

Table 11. Formulas used to compute input features of hardness and yield strength models.

Feature Description	Formula
Difference in Pauling electronegativity	$\Delta x_{pauling} = \sqrt{\sum_{i=1}^n C_i (x_i - \bar{x})^2}$ $\bar{x} = \sum_{i=1}^n C_i x_i$ <p><math>x_i</math> – Pauling Electronegativity of element  <math>C_i</math> – Molar ratio of each element</p>
Difference in Allen electronegativity	$\Delta x_{allen} = \sqrt{\sum_{i=1}^n C_i (x_i - \bar{x})^2}$ $\bar{x} = \sum_{i=1}^n C_i x_i$ <p><math>x_i</math> – Allen Electronegativity of element  <math>C_i</math> – Molar ratio of each element</p>
Mixing Entropy	$S_{mix} = -8.314 \sum_{i=1}^n C_i \ln C_i$ <p><math>C_i</math> – Molar ratio of each element</p>
Mixing Enthalpy	$H_{mix} = 4 \sum_{i=1, j>i}^n C_i C_j H_{i-j}^{mix}$ <p><math>C_i, C_j</math> – Molar ratio of each element</p>
Difference in Atomic Radii	$\delta = \sqrt{\sum_{i=1}^n C_i \left(1 - \frac{r_i}{\bar{r}}\right)^2}$ $\bar{r} = \sum_{i=1}^n C_i r_i$ <p><math>r_i</math> – Atomic Radii of element  <math>C_i</math> – Molar ratio of each element</p>
Difference in Lattice Constants	$\Delta a = \sqrt{\sum_{i=1}^n C_i (a_i - \bar{a})^2}$ $\bar{a} = \sum_{i=1}^n C_i a_i$ <p><math>a_i</math> – Lattice Constant of element  <math>C_i</math> – Molar ratio of each element</p>
Difference in melting Temperature	$\Delta T_m = \sqrt{\sum_{i=1}^n C_i (T_i - \bar{T})^2}$ $\bar{T} = \sum_{i=1}^n C_i T_i$ <p><math>T_i</math> – Melting Temperature of element  <math>C_i</math> – Molar ratio of each element</p>

Feature Description	Formula
Parameter - $\lambda$	$\lambda = \frac{S_{mix}}{\delta^2}$
Parameter - $\Omega$	$\Omega = \frac{T_m S_{mix}}{ \Delta H_{mix} }$
Average Lattice Constant	$a_m = \sum_{i=1}^n C_i a_i$ <p><math>a_i</math> – Lattice Constant of element  <math>C_i</math> – Molar ratio of each element</p>
Valence Electron Concentration	$VEC = \sum_{i=1}^n C_i VEC_i$ <p><math>VEC_i</math> – VEC of element  <math>C_i</math> – Molar ratio of each element</p>
Difference in Shear Modulus	$\Delta G = \sqrt{\sum_{i=1}^n C_i (G_i - \bar{G})^2}$ <p><math>G_i</math> – Shear Modulus of element  <math>C_i</math> – Molar ratio of each element</p> $\bar{G} = \sum_{i=1}^n C_i G_i$
Average Shear Modulus	$G_m = \sum_{i=1}^n C_i G_i$ <p><math>G_i</math> – Shear Modulus of element  <math>C_i</math> – Molar ratio of each element</p>

The Neural network constructed to train two separate models for predicting hardness and yield strength is a fully connected network consisting of sequence of layers. A sequential model is created by adding one layer at a time, the Neural model has total of five layers. The 14 computed features from Table 11, namely - difference in Pauling electronegativity, difference in Allen electronegativity, mixing entropy, mixing enthalpy, difference in atomic radii, difference in lattice constants, difference in melting temperature, average lattice constant, valence electron concentration, difference in shear modulus, average shear modulus and parameter— $\lambda$ ,  $\Omega$  are passed on as input to the first layer. The first two hidden layers have 32 nodes each, followed by two more layers having 16 nodes each. All the four hidden layers have rectified linear unit (ReLU) activation function. The fifth layer is the output layer having one node for the hardness. The neural network is compiled using mean squared loss as loss function and Adam optimizer. Once the neural network is defined and compiled, the training is done on a training data and then tested on the test data to measure the performance of the model on the said data.

The Hardness dataset consisting of hardness data for 243 MPEAs is split into training and test data containing 202 MPEAs and 41 MPEAs respectively. Similarly, the yield strength dataset consisting of yield strength data for 160 MPEAs is split into training and test data containing 128 MPEAs and 32 MPEAs respectively. The training data is used to train the hardness model and the model performance was gauged using the test data. The coefficient of determination ( $R^2$ ) is used to measure the performance of neural network trained on the test data. Table 12 contains

details on the performance of hardness and yield strength neural models on the reserved test data.

Table 12. Performance of hardness and yield strength models.

Model	R <sup>2</sup> Accuracy
Hardness Neural Model	84.09 %
Yield Strength Neural Model	61.49 %

### 3.3 Multi Objective Bayesian Optimization

Bayesian optimization is a technique used for optimization of black box function. A black box is system whose internal working are unknown and the only available information on hand is the input and the output to the box. Bayesian optimization helps in optimizing this unknown function which is also referred to as the objective of the optimization. In this study, the multi objective Bayesian optimization (MOBO) problem involves optimizing multiple objectives to develop new alloy composition in the elemental space of Fe-Cr-Cu-Al-Nb-Ta-Ti-V-Zr-Mo-W-Mn by maximizing hardness and yield strength simultaneously. In a multiple objective optimization problem, both the objectives compete (i.e., when one objective is maximized or minimized the other objective suffers and vice versa). Hence a multiple objective optimization generally involves reaching a compromise or trade-off between both the objectives. This set of compromised or non-dominated solutions are referred as Pareto front (Shi et al., 2023).

MOBO consists of two parts – first to develop a surrogate model (typically Gaussian process model is used) to fit the known data available and predict outcome in unknown space. The surrogate model computes a posterior probability distribution. This distribution is an estimate of the data and includes the uncertainty associated with the distribution too (Ghorbani et al., 2024; Schulz et al., 2017). The second part to MOBO being designing an acquisition function to deduce the new set of candidates and evaluate the target property based on known information available through posterior distribution. An acquisition function finds the new candidates by balancing the exploration of unknown regions and exploitation of regions which maximizes the target objectives (Brochu et al., 2010; Rasmussen, et al., 2003).

A dataset is curated from literature containing hardness and yield strength data for 201 MPEAs (Gorsse et al., 2018; Li et al., 2023) included in Appendix B3. This curated dataset is contained in a 23-element space namely Ni-Co-Fe-Cr-Cu-Al-Nb-Ta-Ti-V-Zr-Hf-Mo-Si-W-Re-C-Y-Sn-Pd-Mn-Sc-Zn. The mole fraction of elements contained in each of 210 MPEAs is computed and passed on as inputs to MOBO model developed.

In this study MOBO is implemented to maximize the hardness and yield strength using BoTorch. BoTorch is a Python framework developed by Facebook built on top of PyTorch. It contains APIs which aids in implementing single and multi-objectives Bayesian problems. Two surrogate model are implemented to fit one each for hardness and yield strength using SingleTaskGP API, then both the surrogate models are combined to one multi-output model using ModelListGP where each target property is modeled independently. The acquisition function is then implemented using parallel Expected Hypervolume Improvement (qEHVI) (Daulton et al., 2020) to generate new composition with objective of optimizing maximizing hardness and yield strength into one. The hypervolume is defined as Lebesgue measure dominated by a certain Pareto front and bounded below by a reference point (Shi et al., 2023). The new candidate/ composition performance on Pareto front is evaluated through hypervolume improvement (HVI)

(i.e., solutions on pareto front should have a higher hypervolume and all the solution on pareto front should have similar hypervolume contribution to be considered as non-dominated solutions). The new alloy composition generated using MOBO is being explored in a reduced elemental space of Fe-Cr-Cu-Al-Nb-Ta-Ti-V-Zr-Mo-W-Mn. It is implemented by setting the bounds of the above elements to be within 0 to 1 (representing the mole fractions of each element) and the other elements to be 0 and a linearly constrained for the total mole fraction of all elements in new alloy being generated to add up to 1. For the new alloy composition obtained through MOBO, 14 features from Table 11 are computed and its hardness and yield strength value are computed using the hardness and yield strength model respectively. This newly generated data point with its computed hardness and yield strength values are appended to the original dataset of 201 MPEAs. The posterior probability distribution of surrogate models is updated, and the acquisition function uses the updated model to determine the next point to evaluate. This cyclic process of adding the new composition to training data, updating surrogate model, and querying the next sample is repeated for 200 iterations, each iteration generates 4 new compositions in parallel using batch optimization technique. A total of 800 new compositions are generated and after plotting the hardness and yield strength objectives, 3 compositions are found in the Pareto front. Figure 28 contains the hardness and yield strength of old MPEAs and new MPEAs plotted together. Table 13 contains details about these three compositions on Pareto front.

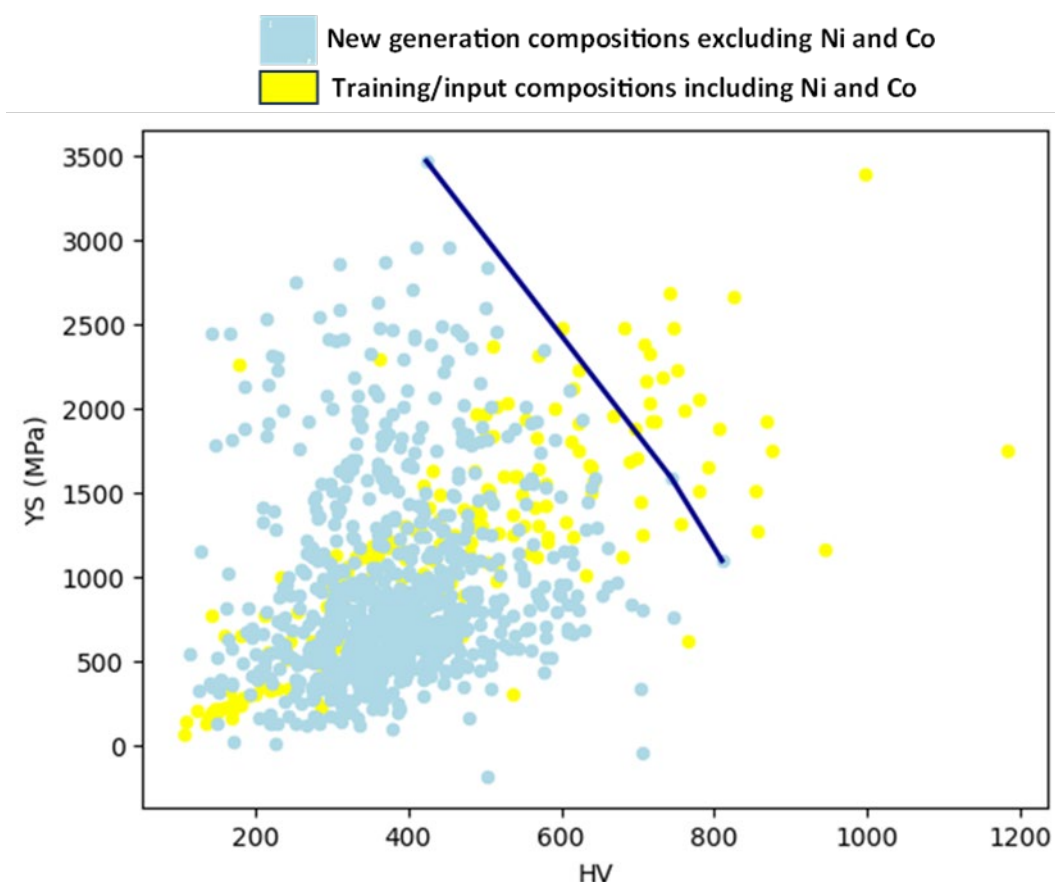


Figure 28. Hardness versus yield strength of the alloys in original training data represented using yellow dots and new compositions suggested by Bayesian optimization represented using blue dots. The solid blue line represents the alloys in the Pareto front.

Table 13. Details of 3 composition on the Pareto front and their predicted hardness and yield strength (YS).

Fe	Cr	Cu	Al	Nb	Ta	Ti	V	Zr	Mo	W	Mn	Pred HV	Pred. YS
0.122	0.046	0.006	0.001	0.080	0.071	0.077	0.068	0.100	0.234	0.175	0.0199	424	3468
0.223	0.331	0.046	0.027	0.009	0.031	0.141	0.068	0.013	0.102	0.010	0.0003	744	1589
0.240	0.020	0.027	0.036	0.091	0.077	0.021	0.005	0.100	0.040	0.342	0.0005	810	1097

### 3.4 Next Actions

The predictions made through MOBO need to be verified by conducting simulations using molecular dynamics and by experimentally developing the alloys and measuring their hardness and yield strength values. Moreover, the MOBO model as well as the models to predict hardness and yield strength needs to be further optimized. Current neural models developed for predicting hardness and yield strength are not very high performing models, hence the predicted hardness and yield strength values have a higher prediction uncertainty associated with them. To derive more reliable and accurate predictions, the aim is to explore other tree-based ensemble models, kernel models in future work. The accuracy of these hardness and yield strength models has a major impact on the MOBO model too, for the new composition generated we need the predictions to be as close to accurate as possible and a higher uncertainty might hinder the predictions and the overall performance obtained from MOBO. The current MOBO model just takes the mole fraction ratio as inputs to the model, whereas the hardness and yield strength models take 14 features in Table 11 as inputs to their model. These inconsistencies in inputs given to MOBO and the hardness and yield strength neural models might also be hampering the overall performance of MOBO. In future work, developing models having consistent inputs to MOBO, hardness and yield strength models needs to be explored. There are many of new acquisition functions that can be explored in MOBO in addition to qEHVI acquisition function, like Upper Confidence Bound (UCB); Mutual Information (MI); parallel Noisy Expected Hypervolume Improvement (qNEHVI) (Daulton et al., 2021); and many more. Overall, the MOBO model developed in this study is in its nascent stage of implementation and needs further optimization to derive more reliable new compositions from it.

## 4.0 Conclusions and Recommendations

A computational feasibility study of modifications to the composition of IN617, with the addition of Mn and the reduction of the Co content, reducing the demand on critical minerals has been reported here. The results of this MD study were used to downselect one alloy formulation that was experimentally produced by two methods, casting and FSA and the resulted metal alloy was characterized. FSA produced a finer grain alloy with an enhance Vickers hardness under the experimental conditions used for this report. Both methods produced alloys that formed FCC phases confirmed by XRD (cast alloy) and EBSD (FSA run#1 alloy). The cast IN617-M1 alloy had comparable hardness values of solution annealed IN617 and slightly lower values of as-cast IN617 produced at PNNL (van Rooyen et al, 2024), despite the significantly larger grain sizes observed. Both alloys produced in this study either showed nearly equivalent or increased strength relative to IN617, an acceptable outcome that demonstrates the potential for new alloys suitable for nuclear applications. Additional testing of the alloy suggested through computer modeling may be required to understand the accuracy of the model. These variations can help optimize the alloy further and validate and help refine the model. Further mechanical property testing on MD informed compositions are required to confirm Vickers hardness values relate, as expected to tensile strength. IN617-M1 shows considerable promise as a material, particularly when subjected to advanced processing methods like friction stir alloying (FSA) due to the grain refinement as an additional strengthening mechanism.

The multi objective Bayesian optimization (MOBO) work presented in this study used to develop new alloys without the critical minerals nickel and cobalt has shown promise. Developing models with consistent inputs to MOBO, hardness and yield strength models needs to be explored in the future. Predictions made through MOBO need to be verified by conducting simulations using molecular dynamics and by experimentally producing the alloys and measuring their hardness and yield strength values.

## 5.0 Reports, Publications and Presentations

Three reports resulted to date from this project:

- M3CR-22PN0401013, Nuclear energy critical material waste minimization enabled by AM techniques, May 2024
- M2CR-22PN0401015, Summary: Nuclear Energy critical materials waste reduction and supply chain solutions enabled by advanced manufacturing, September 2024

Two conference presentations resulted to date from this project:

- Chinthaka Silva, Ankit Roy, Carlyne Burns, Benjamin Lund, Steven Livers, Thomas Hartman, Mohan Nartu, Subhashish Meher, Isabella van Rooyen, Development of Nuclear Reactor Structural Materials with Low Critical Mineral Concentrations, MS&T2024 MS&T24: Where Materials Innovation Happens, October 6–9, 2024 | David L. Lawrence Convention Center | Pittsburgh, Pennsylvania, USA
- Isabella van Rooyen, Thomas Hartman, Praveen K. Thallapally, Chinthaka Silva, Ankit Roy, Subhashish Meher, Jorge Dos Santos, Carlyne Burns, Ben Lund, Steven Slivers, Impact of Additive Manufacturing Technologies on Critical Mineral Usage and Waste for Nuclear Structural Materials, ASTM International Conference on Advanced Manufacturing 2024 (ICAM2024), October 28, 2024 -November 01, 2024

## 6.0 References

- An, XH, SD Wu, ZF Zhang, RB Figueiredo, N Gao, and TG Langdon. 2010. "Evolution of Microstructural Homogeneity in Copper Processed by High-Pressure Torsion." *Scripta Materialia* 63, no. 5: 560-63.
- Bandura, AV, and JD Kubicki. 2003. "Derivation of Force Field Parameters for Tio<sub>2</sub>- H<sub>2</sub>o Systems from Ab Initio Calculations." *The Journal of Physical Chemistry B* 107, no. 40: 11072-81.
- Brochu, Eric, Vlad M Cora, and Nando De Freitas. 2010. "A Tutorial on Bayesian Optimization of Expensive Cost Functions, with Application to Active User Modeling and Hierarchical Reinforcement Learning." *arXiv preprint arXiv:1012.2599*.
- Broitman, E. 2017. Indentation Hardness Measurements at Macro-, Micro-, and Nanoscale: A Critical Overview. *Tribol Lett* 65, 23. <https://doi.org/10.1007/s11249-016-0805-5>
- Couzinié, J. P., O. N. Senkov, D. B. Miracle, and G. Dirras. 2018. "Comprehensive Data Compilation on the Mechanical Properties of Refractory High-Entropy Alloys." *Data in Brief* 21: 1622-41. <https://doi.org/10.1016/j.dib.2018.10.071>
- Daulton, Samuel, Maximilian Balandat, and Eytan Bakshy. 2020. "Differentiable Expected Hypervolume Improvement for Parallel Multi-Objective Bayesian Optimization." *Advances in Neural Information Processing Systems* 33: 9851-64.
- Daulton, Samuel, Maximilian Balandat, and Eytan Bakshy. 2021. "Parallel Bayesian Optimization of Multiple Noisy Objectives with Expected Hypervolume Improvement." *Advances in Neural Information Processing Systems* 34: 2187-200.
- DOE. 2021. *Critical Minerals and Materials: U.S. Department of Energy's Strategy to Support Domestic Critical Mineral and Material Supply Chains (FY 2021–FY 2031)*. Department of Energy. Washington, DC.
- Georgieva, Violeta, M Saraiva, Neeru Jehanathan, OI Lebelev, Diederik Depla, and Annemie Bogaerts. 2009. "Sputter-Deposited Mg–Al–O Thin Films: Linking Molecular Dynamics Simulations to Experiments." *Journal of Physics D: Applied Physics* 42, no. 6: 065107.
- Ghorbani, M., M. Boley, P. N. H. Nakashima, and N. Birbilis. 2024. "An Active Machine Learning Approach for Optimal Design of Magnesium Alloys Using Bayesian Optimisation." *Scientific Reports* 14, no. 1: 8299. <https://doi.org/10.1038/s41598-024-59100-9>
- Gorsse, S., M. H. Nguyen, O. N. Senkov, and D. B. Miracle. 2018. "Database on the Mechanical Properties of High Entropy Alloys and Complex Concentrated Alloys." *Data in Brief* 21: 2664-78. <https://doi.org/10.1016/j.dib.2018.11.111>
- Gröger, R, V Vitek, and A Dlouhý. 2020. "Effective Pair Potential for Random Fcc Cocrfemnni Alloys." *Modelling and Simulation in Materials Science and Engineering* 28, no. 7: 075006. DOI: [10.1088/1361-651x/ab7f8b](https://doi.org/10.1088/1361-651x/ab7f8b).
- Gusieva, K, CHJ Davies, JR Scully, and N Birbilis. 2015 "Corrosion of Magnesium Alloys: The Role of Alloying." *International Materials Reviews* 60, no. 3: 169-94.

Hartmann, T., S. Maloy, I. J. van Rooyen. 2022. *Critical Minerals Evaluation Report – Advanced Materials and Manufacturing Technology*. Pacific Northwest National Laboratory PNNL-33356. Richland, WA.

Hartmann, T., P. K. Thallapally, I. J. van Rooyen. 2023. *Strategic Plan: Decrease Critical Minerals Waste through Enabling Advanced Manufacturing Techniques*. Pacific Northwest National Laboratory PNNL-34225. Richland, WA.

Hermet, J, G Geneste, and G Dezanneau. 2010. "Molecular Dynamics Simulations of Oxygen Diffusion in Gdbaco2o5. 5." *Applied Physics Letters* 97, no. 17.

Krishna, R., S. V. Hainsworth, H. V. Atkinson and A. Strang. 2010 "Microstructural analysis of creep exposed IN617 alloy" *Materials Science and Technology* Vol 26: No 7, 797-802  
<https://doi.org/10.1179/026708309X12584564052094>

Khakurel, Hrishabh, M. F. N. Taufique, Ankit Roy, Ganesh Balasubramanian, Gaoyuan Ouyang, Jun Cui, Duane D. Johnson, and Ram Devanathan. 2021. "Machine Learning Assisted Prediction of the Young's Modulus of Compositionally Complex Alloys." *Scientific Reports* 11, no. 1: 17149. <https://doi.org/10.1038/s41598-021-96507-0>

Li, Hongqi, and Fereshteh Ebrahimi. 2003. "Synthesis and Characterization of Electrodeposited Nanocrystalline Nickel–Iron Alloys." *Materials Science and Engineering: A*, 347, no. 1-2: 93-101. [https://doi.org/10.1016/S0921-5093\(02\)00586-5](https://doi.org/10.1016/S0921-5093(02)00586-5)

Li, Z., S. Li, and N. Birbilis. 2024. "A Machine Learning-Driven Framework for the Property Prediction and Generative Design of Multiple Principal Element Alloys." *Materials Today Communications* 38: 107940. <https://doi.org/10.1016/j.mtcomm.2023.107940>

Li, Z., Z. R. Zeng, R. Tan, M. L. Taheri, and N. Birbilis. 2023. "A Database of Mechanical Properties for Multi Principal Element Alloys." *Chemical Data Collections* 47: 101068. <https://doi.org/10.1016/j.cdc.2023.101068>

Maphanga, RR, SC Parker, and PE Ngoepe. 2009. "Atomistic Simulation of the Surface Structure of Electrolytic Manganese Dioxide." *Surface science* 603, no. 21: 3184-3190. <https://doi.org/10.1016/j.susc.2009.07.038>

McKee, D. W. and R. G. Frank, 1981, "Corrosion Behavior of Experimental Alloys in Controlled Purity Helium," IAEA Specialists Meeting on High Temperature Metallic Materials for Application in Gas-Cooled Reactors, Vienna, Austria, May 4-6, 1981, Report IWGGCR-4, Paper I1.

Minervini, Licia, Matthew O Zacate, and Robin W Grimes. 1999. "Defect Cluster Formation in M2o3-Doped Ceo2." *Solid State Ionics* 116, no. 3-4: 339-49.

Natesan, A.P.K., S.W. Tam. 2003. "Materials Behavior in HTGR Environments." NUREG/CR-6824/ANL-02/37 U.S. Nuclear Regulatory Commission, Washington, DC 20555-0001

Plimpton, Steve. 1995. "Fast Parallel Algorithms for Short-Range Molecular Dynamics." *Journal of computational physics* 117, no. 1: 1-19. <https://doi.org/10.1006/jcph.1995.1039>

Qiu, Yao, Sebastian Thomas, Mark A Gibson, Hamish L Fraser, and Nick Birbilis. 2017. "Corrosion of High Entropy Alloys." *npj Materials degradation* 1, no. 1: 1-18.

- Rai, Arun Kumar, Haraprasanna Trpathy, R. N. Hajra, S. Raju, and S. Saroja. 2017. "Thermophysical Properties of Ni Based Super Alloy 617." *Journal of Alloys and Compounds* 698: 442-50. <https://doi.org/10.1016/j.jallcom.2016.12.183>
- Rajaramakrishna, R, Pattarapong Nijapai, Pinit Kidkhunthod, HJ Kim, J Kaewkhao, and Y Ruangtaweep. 2020. "Molecular Dynamics Simulation and Luminescence Properties of Eu<sup>3+</sup> Doped Molybdenum Gadolinium Borate Glasses for Red Emission." *Journal of Alloys and Compounds* 813: 151914.
- Rasmussen, C.E. (2004). Gaussian Processes in Machine Learning. In: Bousquet, O., von Luxburg, U., Rätsch, G. (eds) *Advanced Lectures on Machine Learning. ML 2003. Lecture Notes in Computer Science()*, vol 3176. Springer, Berlin, Heidelberg. [https://doi.org/10.1007/978-3-540-28650-9\\_4](https://doi.org/10.1007/978-3-540-28650-9_4)
- Restrepo, Óscar A, Óscar Arnache, J Restrepo, Charlotte S Becquart, and Normand Mousseau. 2022. "Comparison of Bulk Basic Properties with Different Existing Ni-Fe-O Empirical Potentials for Fe<sub>3</sub>O<sub>4</sub> and NiFe<sub>2</sub>O<sub>4</sub> Spinel Ferrites." *Computational Materials Science* 213: 111653. <https://doi.org/10.1016/j.commatsci.2022.111653>
- Roy, Ankit, Ram Devanathan, Duane D Johnson, and Ganesh Balasubramanian. 2022. "Grain-Size Effects on the Deformation in Nanocrystalline Multi-Principal Element Alloy." *Materials Chemistry and Physics* 277: 125546. <https://doi.org/10.1016/j.matchemphys.2021.125546>
- Roy, Ankit, M. F. N. Taufique, Hrishabh Khakurel, Ram Devanathan, Duane D. Johnson, and Ganesh Balasubramanian .2022. "Machine-Learning-Guided Descriptor Selection for Predicting Corrosion Resistance in Multi-Principal Element Alloys." *Materials Degradation* 6, no. 1: 9. <https://doi.org/10.1038/s41529-021-00208-y>
- Schulz, Eric, Maarten Speekenbrink, and Andreas Krause. 2017. "A Tutorial on Gaussian Process Regression: Modelling, Exploring, and Exploiting Functions." *bioRxiv* : 095190. <https://doi.org/10.1101/095190>
- Sharma, Aayush, and Ganesh Balasubramanian. 2017. "Dislocation Dynamics in Al<sub>0.1</sub>CoCrFeNi High-Entropy Alloy under Tensile Loading." *Intermetallics* 91: 31-34. <https://doi.org/10.1016/j.intermet.2017.08.004>
- Shi, Bofeng, Turab Lookman, and Dezhen Xue. 2023. "Multi-Objective Optimization and Its Application in Materials Science." *Materials Genome Engineering Advances* 1, no. 2: e14. <https://doi.org/10.1002/mgea.14>
- Singh, Prashant, Aayush Sharma, Andrei V Smirnov, Mouhamad S Diallo, Pratik K Ray, Ganesh Balasubramanian, and Duane D Johnson. 2018. "Design of High-Strength Refractory Complex Solid-Solution Alloys." *npj Computational Materials* 4, no. 1: 16.
- Solomou, Alexandros, Guang Zhao, Shahin Boluki, Jobin K. Joy, Xiaoning Qian, Ibrahim Karaman, Raymundo Arróyave, and Dimitris C. Lagoudas. 2018. "Multi-Objective Bayesian Materials Discovery: Application on the Discovery of Precipitation Strengthened NiTi Shape Memory Alloys through Micromechanical Modeling." *Materials & Design* 160: 810-27. <https://doi.org/https://doi.org/10.1016/j.matdes.2018.10.014>

- Stukowski, A. 2009. "Visualization and analysis of atomistic simulation data with OVITO—the Open Visualization Tool." *Modelling and Simulation in Materials Science and Engineering* 18(1):015012. <http://doi.org/10.1088/0965-0393/18/1/015012>
- Takeuchi, Akira, and Akihisa Inoue. 2005. "Classification of Bulk Metallic Glasses by Atomic Size Difference, Heat of Mixing and Period of Constituent Elements and Its Application to Characterization of the Main Alloying Element." *Materials transactions* 46, no. 12: 2817-29.
- Taufique, MFN, O Mamun, A Roy, H Khakurel, G Balasubramanian, G Ouyang, J Cui, DD Johnson, and R Devanathan. 2024. "Machine Learning Guided Prediction of the Yield Strength and Hardness of Multi-Principal Element Alloys [Version 2; Peer Review: 2 Approved, 2 Approved with Reservations]." *Materials Open Research* 2, no. 9. <https://doi.org/10.12688/materialsopenres.17476.2>. <https://materialsopenresearch.org/articles/2-9/v2>
- Thermo-Calc Software TCFE13 Steels/Fe-alloys Database  
<https://thermocalc.com/products/databases/steel-and-fe-alloys/>
- Thermo-Calc Software TCHEA7 High Entropy Alloys Database  
<https://thermocalc.com/products/databases/high-entropy-alloys/>
- Totemeier, Terry C, and Hongbo Tian. 2007. "Creep-Fatigue–Environment Interactions in Inconel 617." *Materials Science and Engineering: A* 468: 81-87. <https://doi.org/10.1016/j.msea.2006.10.170>
- US Office of Nuclear Energy. 2020. "New Alloy Material Approved for Use in High-Temperature Nuclear Plants" Accessed August 8, 2024. <https://www.energy.gov/ne/articles/new-alloy-material-approved-use-high-temperature-nuclear-plants>
- van Rooyen I., S. Meher, P.K. Thallapally, J. Fernandez dos Santos, C.M. Silva, S. Shin, and T. Wang, et al. 2024. *Nuclear Energy Critical Material Waste Minimization Enabled by AM Techniques*. PNNL-36049. Richland, WA: Pacific Northwest National Laboratory.
- Wang, Yue, Qu Liu, Zhipeng Cai, Haitao Wang, Li Shi, and Kejian Li. 2023. "Nitride Precipitation and Formation in In617 Superalloy During Creep." *Journal of Alloys and Compounds* 948: 169709.
- Wen, Cheng, Yan Zhang, Changxin Wang, Dezhen Xue, Yang Bai, Stoichko Antonov, Lanhong Dai, Turab Lookman, and Yanjing Su. 2019. "Machine Learning Assisted Design of High Entropy Alloys with Desired Property." *Acta Materialia* 170: 109-17. <https://doi.org/10.1016/j.actamat.2019.03.010>
- Wen, Yu-Hua, Zi-Zhong Zhu, and Ru-Zeng Zhu. 2008. "Molecular Dynamics Study of the Mechanical Behavior of Nickel Nanowire: Strain Rate Effects." *Computational Materials Science* 41, no. 4: 553-60. <https://doi.org/10.1016/j.commatsci.2007.05.012>
- Zhang, Peng, SX Li, and ZF Zhang. 2011. "General Relationship between Strength and Hardness." *Materials Science and Engineering: A* 529: 62-73. <https://doi.org/10.1016/j.msea.2011.08.061>

Zhou, XW, RA Johnson, and HNG Wadley. 2004. "Misfit-Energy-Increasing Dislocations in Vapor-Deposited CoFe/NiFe Multilayers." *Physical Review B* 69, no. 14: 144113.  
<https://doi.org/10.1103/PhysRevB.69.144113>

## Appendix A Datasets Used for MOBO

### A.1 Hardness Dataset

Alloy	Yield Strength (MPa)
CoFeNiSi0.75	1301
Al0.75CoFeNi	794
AlCoCrFeNi	1251
AlC0.1CoCrFeNi	957
AlC0.2CoCrFeNi	906
AlC0.3CoCrFeNi	867
AlC0.4CoCrFeNi	1056
AlC0.5CoCrFeNi	1060
AlCCoCrFeNi	1251
AlC1.5CoCrFeNi	1255
AlCoCrFeMo0.1Ni	1804
AlCoCrFeMo0.2Ni	2456
AlCoCrFeMo0.3Ni	2649
AlCoCrFeMo0.4Ni	2670
AlCoCrFeMo0.5Ni	2757
AlCoCrFeNb0.1Ni	1641
AlCoCrFeNb0.25Ni	1959
AlCoCrFeNb0.5Ni	2473
AlCoCrFeNiSi0.2	1265
AlCoCrFeNiSi0.4	1481
AlCoCrFeNiSi0.6	1834
AlCoCrFeNiSi0.8	2179
AlCoCrFeNiSi	1110
AlCoCrFeNiTi0.5	2260
CoCrFeMnNiV0.5	620
CoCrFeMnNiV0.75	740
CoCrFeMnNiV1.0	1660
AlCrFeNi	1406
AlCrFeNiMo0.2	1487
AlCrFeNiMo0.5	1749
AlCrFeNiMo0.8	1513
CoCrCuFeNiTi0.5	700

<b>Alloy</b>	<b>Yield Strength (MPa)</b>
CoCrCuFeNiTi	1272
Al0.25CoCrCu0.75FeNiTi	750
AlCoCrCuFeNi	1303
AlCoCrCuFeMnNi	1005
AlCoCrCuFeNiTi	1234
AlCoCrCuFeNiV	1469
Al2CoCrCuFeNi	1620
AlCoFeNi	964
Al1.125CuFe0.75NiTi1.1	980
Al22.5Cu20Fe15Ni20Ti2	980
AlCuFeNiTi	1074
TaNbHfZrTi	929
Al0.25MoNbTiV	1250
Al0.25NbTaTiV	1330
Al0.2MoTaTiV	1021
Al0.3HfNbTaTiZr	1188
Al0.3NbTa0.8Ti1.4V0.2Zr1.3	1965
Al0.4Hf0.6NbTaTiZr	1841
Al0.5CrNbTi2V0.5	1240
Al0.5HfNbTaTiZr	1302
Al0.5MoNbTiV	1625
Al0.5NbTa0.8Ti1.5V0.2Zr	2035
Al0.5NbTaTiV	1012
Al0.6MoTaTiV	962
Al0.75HfNbTaTiZr	1415
Al0.75MoNbTiV	1260
Al1.5MoNbTiV	500
AlCr0.5NbTiV	1300
AlMoNbTiV	1375
AlMoTaTiV	735
AlNb1.5Ta0.5Ti1.5Zr0.5	1280
AlNbTaTiV	991
AlNbTiV	1000
CoCrMoNbTi0.4	1771.3
Hf0.4Nb1.54Ta1.54Ti0.89Zr0.64	882
Hf0.5Mo0.5NbTiZr	1176

<b>Alloy</b>	<b>Yield Strength (MPa)</b>
Hf0.5Nb0.5Ta0.5Ti1.5Zr	903
Hf0.75NbTa0.5Ti1.5Zr1.25	1100
HfMo0.25NbTaTiZr	1112
HfMo0.5NbTaTiZr	1137
HfMo0.5NbTiV0.5	1260
HfMoNbTaTiZr	1512
HfMoNbTiZr	1719
HfMoTaTiZr	1600
HfNb0.18Ta0.18Ti1.27Zr	540
HfNbTaTiZr	1073
HfNbTaZr	1315
HfNbTiVZr	1253
HfNbTiZr	879
HfTaTiZr	1500
Mo0.1NbTiV0.3Zr	932
Mo0.3NbTiV0.3Zr	1312
Mo0.3NbTiVZr	1289
Mo0.5NbTiV0.3Zr	1301
Mo0.5NbTiVZr	1473
Mo0.7NbTiV0.3Zr	1436
Mo0.7NbTiVZr	1706
Mo1.3NbTiV0.3Zr	1603
Mo1.3NbTiVZr	1496
Mo1.5NbTiV0.3Zr	1576
MoNbTaTi0.25W	1109
MoNbTaTi0.5W	1211
MoNbTaTi0.75W	1304
MoNbTaTiV	1400
MoNbTaTiVW	1515
MoNbTaTiW	1455
MoNbTaV	1525
MoNbTaVW	1246
MoNbTaW	1058
MoNbTiV	1200
MoNbTiV0.25Zr	1750
MoNbTiV0.3Zr	1455

<b>Alloy</b>	<b>Yield Strength (MPa)</b>
MoNbTiV0.5Zr	1640
MoNbTiV0.75Zr	1680
MoNbTiVZr	1779
MoNbTiZr	1560
MoTaTiV	1221
NbTaTiV	1092
NbTaTiVW	1420
NbTaVW	1530
NbTiV0.3Zr	866
NbTiVZr	1105
AlMo0.5NbTa0.5TiZr	2000
Al0.3NbTaTi1.4Zr1.3	1965
NbTiV2Zr	918
CrHfNbTiZr	1375
CrMo0.5NbTa0.5TiZr	1595
CrNbTiVZr	1298
Hf0.5Mo0.5NbTiZr	1178
Hf0.5Mo0.5NbSi0.1TiZr	1365
Hf0.5Mo0.5NbSi0.3TiZr	1428
Hf0.5Mo0.5NbSi0.5TiZr	1605
Hf0.5Mo0.5NbSi0.7TiZr	1604
Hf0.5Mo0.5NbSi0.9TiZr	1677
Hf0.5Mo0.5NbTiZrCr0.1	1183
Hf0.5Mo0.5NbTiZrCr0.3	1201
HfNbSi0.5TiV	1399
HfNbSi0.5TiVZr	1540
HfNbTiVZr	1170
CoCrCuFeMnNiTiV	1312
Cu30Mn30Ni30Al10	515
Cu30Mn30Ni30Sn11	630
AlCrFeNiMo0.5	1914.1
AlCrFeNiMo0.5Ti0.25	2161.7
AlCrFeNiMo0.5Ti0.4	2185.1
AlCrFeNiMo0.5Ti0.5	2228.7
AlCrFeNiMo0.5Ti0.6	1314.5
AlCrFeNiMo0.5Ti0.75	618.8

Alloy	Yield Strength (MPa)
HfMo0.5NbTaTiZr	1317
HfMo0.75NbTaTiZr	1373
HfMoNbZrTi	1803
Mo1.7NbTiVZr	1645
Mo2NbTiVZr	1765
MoNbTiV1.0Zr	1786
MoNbTiV1.5Zr	1735
MoNbTiV2.0Zr	1538
MoNbTiV3.0Zr	1418
MoNbTiZr	1592
Nb5V20Cr60W5Ta5Al5	1474
Nb10V25Cr50W5Ta5Al5	1401
Mo5V25Cr55W5Ta5Al5	1511
Mo10V35Cr40W5Ta5Al5	1471
Mo15V40Cr30W5Ta5Al5	1470
Mo20Nb10V30Cr25W5Ta5Al5	1458
Mo20Nb40Cr25W5Ta5Al5	1403
Mo40Nb35Cr10W5Ta5Al5	1525
Mo50Nb10V20Cr5W5Ta5Al5	1658
Mo55Nb5V5Cr20W5Ta5Al5	1748

## A.2 Hardness Dataset

Alloy	Hardness (Vickers)
CoFeNi	125
CoFeNiSi0.25	149
CoFeNiSi0.5	287
CoFeNiSi0.75	570
Al0.25CoFeNi	138
Al0.5CoFeNi	212
Al0.75CoFeNi	385
CoCrFeNi	116
CoCrFeMo0.5Ni	210
Co1.5CrFeNi1.5Ti0.5	509
Co1.5CrFeNi1.5Ti	654
Al0.25CoCrFeNi	110

<b>Alloy</b>	<b>Hardness (Vickers)</b>
Al0.5CoCrFeNi	159
Al0.7Co0.3CrFeNi	624
Al0.75CoCrFeNi	388
Al0.875CoCrFeNi	538
AlCoCrFeNi	484
Al1.25CoCrFeNi	499
Al2CoCrFeNi	509
Al2.5CoCrFeNi	487
Al3CoCrFeNi	506
Al0.5CoCrFeMo0.5Ni	425
AlCo0.5CrFeMo0.5Ni	801
AlCoCrFe0.5Mo0.5Ni	755
AlCoCrFe0.6Mo0.5Ni	754
AlCoCrFeMo0.5Ni0.5	708
AlCoCrFeMo0.5Ni	796
AlCoCrFeMo0.5Ni1.5	586
AlCoCrFeMo0.5Ni2	395
AlCo1.5CrFeMo0.5Ni	741
AlCo2CrFeMo0.5Ni1.5	586
AlCo2CrFeMo0.5Ni2	395
AlCo1.5CrFeMo0.5Ni	741
AlCo2CrFeMo0.5Ni	586
AlCoCrFe1.5Mo0.5Ni	635
AlCoCrFe2Mo0.5Ni	639
Al1.5CoCrFeMo0.5Ni	655
Al2CoCrFeMo0.5Ni	605
AlCoCrFeNb0.1Ni	569
AlCoCrFeNb0.25Ni	668
AlCoCrFeNb0.5Ni	747
Al0.2Co1.5CrFeNi1.5Ti0	487
AlCoCrFeNiTi0.5	178
Al2CoCrFeNiTi	643
AlCoCrFeNiTiVZr	780
CoCrFeMnNiV0.25	151
CoCrFeMnNiV0.5	186
CoCrFeMnNiV0.75	342

<b>Alloy</b>	<b>Hardness (Vickers)</b>
Al0.10CoCrFeMnNi	180
Al0.20CoCrFeMnNi	171
Al0.38CoCrFeMnNi	182
Al0.75CoCrFeMnNi	530
Al0.81CoCrFeMnNi	539
Al0.88CoCrFeMnNi	533
Al1.25CoCrFeMnNi	539
Al0.5CrFe1.5MnNi0.5	396
AlCoCrFeMo0.5	857
AlCrFeNi	472
AlCrFeNiMo0.2	549
AlCrFeNiMo0.8	854
CoCrCuFe	134
Al0.3CoCrCuFe	180
Al0.5CoCrCuFe	207
AlCoCrCuFe	407
Al1.5CoCrCuFe	510
Al1.8CoCrCuFe	557
Al2.3CoCrCuFe	603
Al2.5CoCrCuFe	624
Al3CoCrCuFe	644
CoCrCu0.5FeNi	172
CoCrCuFeNi	286
Al0.3CoCrCuFeNi	180
Al0.8CoCrCuFeNi	270
AlCoCrCuFeNi	406
Al1.3CoCrCuFeNi	470
Al1.5CoCrCuFeNi	506
Al1.8CoCrCuFeNi	650
Al2CoCrCuFeNi	560
Al2.3CoCrCuFeNi	600
Al2.5CoCrCuFeNi	620
Al2.8CoCrCuFeNi	650
Al3CoCrCuFeNi	640
Al0.5CoCrCuFeNiTi0.2	272
Al0.5CoCrCuFeNiTi0.4	321

Alloy	Hardness (Vickers)
Al0.5CoCrCuFeNiTi0.6	458
Al0.5CoCrCuFeNiTi0.8	590
Al0.5CoCrCuFeNiTi	636
Al0.5CoCrCuFeNiTi1.4	664
Al0.5CoCrCuFeNiTi1.6	657
Al0.5CoCrCuFeNiTi1.8	667
Al0.5CoCrCuFeNiTi2	696
Al0.5CoCrCuFeNiV0.2	204
Al0.5CoCrCuFeNiV0.6	328
Al0.5CoCrCuFeNiV0.8	447
Al0.5CoCrCuFeNiV1.0	639
Al0.5CoCrCuFeNiV1.2	579
Al0.5CoCrCuFeNiV1.4	577
Al0.5CoCrCuFeNiV1.8	597
AlCoFeNiTiVZr	790
AlCoCuFeNi	536
AlCoCuFeNbNi	578
AlCoCuFeNiSi	682
AlCoCuFeNiTi	626
AlCoCuFeNiZr	472
CoCuFeMnNi	208
CoCuFeMnNiSn0.03	192
CoCuFeMnNiSn0.05	205
CoCuFeMnNiSn0.08	219
CoCuFeMnNiSn0.1	253
CoCuFeMnNiSn0.2	319
CrCuFeMoNi	263
AlCrCuFeNi0.6	496
AlCrCuFeNi0.8	486
AlCrCuFeNi1.0	495
AlCrCuFeNi1.2	407
AlCrCuFeNi1.4	367
Al1.125CuFe0.75NiTi1.1	516
Al22.5Cu20Fe15Ni20Ti2	516
AlCuFeNiTi	516
AlCuNiTi	537

<b>Alloy</b>	<b>Hardness (Vickers)</b>
TaNbHfZrTi	390
Al0.25MoNbTiV	460
Al0.4Hf0.6NbTaTiZr	500
Al0.5HfNbTaTiZr	396
Al0.5MoNbTiV	487
Al0.5NbTa0.8Ti1.5V0.2Zr	530
Al0.75MoNbTiV	517
AlMoNbTiV	537
AlNb1.5Ta0.5Ti1.5Zr0.5	408
AlNbTiV	448
Hf0.5Nb0.5Ta0.5Ti1.5Zr	301
HfMo0.25NbTaTiZr	395
HfMoNbTaTiZr	505
HfMoTaTiZr	542
HfNbTaTiZr	295
HfNbTaZr	365
MoNbTaTi0.25W	478
MoNbTaTi0.75W	496
MoNbTaV	504
MoNbTaVW	536
MoNbTiV	441
NbTiVZr	335
AlMo0.5NbTa0.5TiZr	591
Al0.3NbTaTi1.4Zr1.3	500
HfMo0.75NbTaTiZr	492
NbTiV2Zr	304
CrHfNbTiZr	464
CrMo0.5NbTa0.5TiZr	540
CrNbTiVZr	482
FeMoNiTiVZr	740
Hf0.5Mo0.5NbTiZr	400
Hf0.5Mo0.5NbSi0.1TiZr	442
Hf0.5Mo0.5NbSi0.3TiZr	494
Hf0.5Mo0.5NbSi0.5TiZr	524
Hf0.5Mo0.5NbSi0.9TiZr	640
HfNbSi0.5TiV	490

<b>Alloy</b>	<b>Hardness (Vickers)</b>
HfNbSi0.5TiVZr	464
HfNbTiVZr	388
CoCrCuFeNiTiVZr	680
CoCrCuFeMoNiTiVZr	850
CoCuFeNiTiVZr	630
CoFeNiV	238
CoFeMo0.2NiV	267
CoFeMo0.4NiV	402
CoFeMo0.6NiV	557
CoFeMo0.8NiV	606
CoFeMoNiV	625
CoFeMoNi1.6V	520
CoFeMoNi1.8V	510
CoFeMoNi2V	382
CoFeMoNiTiVZr	790
CuFeNiTiVZr	590
AlFeNiTiVZr	800
Cu25Mn25Ni25Zn25	147
Cu30Mn30Ni30Sn11	318
Cu31.6Mn31.6Ni31.6Al5	166
AlCrFeNiMo0.5	623.7
AlCrFeNiMo0.5Ti0.25	712
AlCrFeNiMo0.5Ti0.4	731.9
AlCrFeNiMo0.5Ti0.5	751.7
AlCrFeNiMo0.5Ti0.6	756.1
AlCrFeNiMo0.5Ti0.75	766.2
Mo85.25Ta9.52Ti2.29Zr2.94	422.2
Mo82.23W1.29Ta9.46Ti3.27Zr3.36Al0.39	429.4
Mo82.93W2Ta9.89Ti2.4Zr2.72Al0.05	410.8
Mo79.73W0.09Ta12.36Ti3.92Zr3.88Cr0.03	479.8
Mo78.53W1.06Ta12.53Ti3.68Zr4.18Cr0.03	492.6
Mo78.58W2.14Ta11.19Ti3.79Zr4.3	480.7
Mo75.86W3.13Ta12.65Ti3.89Zr4.47	517.4
Mo75.66W3.69Ta12.2Ti3.8Zr4.65	501
Mo81.5W1.63Ta6.37Ti3.9Zr4.51Al1.96Cr0.13	526.4
Mo78.86W2.93Ta7.48Ti3.69Zr5.36Cr1.68	445

Alloy	Hardness (Vickers)
Mo79.92Ta9.87Ti4.69Zr5.45Cr0.07	487.1
Mo76.31W0.41Ta9.3Ti6.22Zr7.29Al0.37Cr0.08	497.7
Mo80.87W1.02Ta6.98Ti5.23Zr5.88Al0.03	464.6
Mo76.47W3.17Ta8.64Ti5.25Zr6.45Cr0.02	480.2
Mo71.98W6.62Ta9.97Ti5.06Zr6.32Cr0.06	494.5
Mo78.09W3.06Ta4.93Ti4.92Zr7.9Cr1.1	485.5
Mo78.35W1.61Ta20.03	426.4
Mo75.99W3.83Ta20.18	426.8
Mo74.54W4.2Ta21.25	436.2
Mo77.21W4.17Ta17.69Ti0.34Zr0.07Al0.1Cr0.41	387.5
Al0.375CoCrFeNi	196
Al1.5CoCrFeNi	517
Al0.2Co1.5CrFeNi1.5Ti	717
CoCrFeMnNi	176
CoCrFeMnNiV1.0	650
Al0.43CoCrFeMnNi	183
Al0.49CoCrFeMnNi	220
Al0.56CoCrFeMnNi	278
Al0.62CoCrFeMnNi	405
Al0.68CoCrFeMnNi	486
Al0.95CoCrFeMnNi	535
Al0.3CrFe1.5MnNi0.6	297
AlCrFeNiMo0.5	622
Al0.8CoCrCuFe	271
Al1.3CoCrCuFe	476
Al2CoCrCuFe	567
Al2.8CoCrCuFe	657
Al0.5CoCrCuFeNi	210
Al0.5CoCrCuFeNiTi1.2	646
Al0.5CoCrCuFeNiV0.4	231
Al0.5CoCrCuFeNiV1.6	594
Al0.5CoCrCuFeNiV2.0	587
AlCoFeNi	456
Al0.3HfNbTaTiZr	353
Al0.3NbTa0.8Ti1.4V0.2Zr1.3	490
Al0.75HfNbTaTiZr	427

Alloy	Hardness (Vickers)
MoNbTaTi0.5W	481.2
MoNbTaW	454
MoNbTiV0.3Zr	507.5
HfMo0.5NbTaTiZr	480
Hf0.5Mo0.5NbSi0.7TiZr	580
CoFeMoNi1.2V	602
CoFeMoNi1.4V	538
Cu26.6Mn26.6Ni26.6Zn20	109
Cu30Mn30Ni30Al10	241
Cu31.6Mn31.6Ni31Sn5	205
Mo80.67W3.3Ta10.34Ti2.45Zr3.13Al0.05Cr0.06	411.6
Mo73.77W7.67Ta10.17Ti3.7Zr4.69	473.1
Mo73.61W5.27Ta10.49Ti4.71Zr5.93	513.8
Mo80.03W1.49Ta4.47Ti5.24Zr6.01Al2.73Cr0.04	514
Mo81.65W0.17Ta18.12Ti0.05	436.4

### A.3 Dataset Used for Bayesian Optimization

Alloy	Hardness (Vickers)	Yield Strength (MPa)
Co1Fe1Ni1Si0.5	287	476
Co1Fe1Ni1Si0.75	570	1301
Al1Co1Cr1Fe1Nb0.25Ni1	668	1959
Al1Co1Cr1Fe1Nb0.5Ni1	747	2473
Co1Cr1Fe1Mn1Ni1V0.25	144	200
Co1Cr1Fe1Mn1Ni1V0.75	380	740
Co1Cr1Fe1Mn1Ni1V1	636	1660
Al1Cr1Fe1Ni1	472	1406
Al1Cr1Fe1Mo0.2Ni1	549	1487
Al1Cr1Fe1Mo0.5Ni1	622	1749
Al1Cr1Fe1Mo0.8Ni1	854	1513
Al0.111Cu1Mn1Ni1	241	515
Cu1Mn1Ni1Sn0.111	318	630
Cu1Mn1Ni1Sn0.053	205	380
Al0.278Co0.694Cr0.222Fe0.417Ni1Ti0.167	345	582
Al1Co1Cr1Ni1	1183	1750

Alloy	Hardness (Vickers)	Yield Strength (MPa)
Al1Co0.5Cr0.5Fe0.5Ni0.5	581.7	1241
Al1Co0.556Cr0.556Fe0.556Ni0.556Ti0.111	605.5	1324
Al1Co0.667Cr0.667Fe0.667Ni0.667Ti0.333	641.7	1566
Al1Co0.833Cr0.833Fe0.833Ni0.833Ti0.667	639.6	1503
Al1Co1Cr1Fe1Ni1Ti1	703	1448
Al0.667Co0.83Cr0.833Fe0.833Ni0.833Ti1	856.9	1272
Co1Cr1Fe1Ni1W0.5	357.9	556
Co0.139Cr0.446Cu0.99Ni1Si0.277	142.5	777
Al1Co1Cu1Fe1Ni0.5	430.9	929
Al1Co1Cu1Fe1Ni0.8	420	1021
Al1Co1Cu1Fe1Ni1	391.4	994
Al0.5Co0.5Cu0.5Fe0.5Ni1	299.2	544
Al0.5Cr1Fe1Mn1Ni1	353	1091
Al0.6Cr1Fe1Mn1Ni1	361	1130
Al0.7Cr1Fe1Mn1Ni1	375	1170
Al0.8Cr1Fe1Mn1Ni1	386	1200
Co1Cr1Fe1Mn0.2Ni1Pd1	470	650
Co1Cr1Fe1Mn0.4Ni1Pd1	380	650
Co1Cr1Fe1Mn0.6Ni1Pd1	180	650
Co1Cr1Fe1Mn0.8Ni1Pd1	160	650
Al1Cr1Cu1Fe1Mn1	633	1010
Al1Cr1Cu1Fe1Mn1W0.05	680	1120
Al1Cr1Cu1Fe1Mn1W0.1	705	1250
Al1Cr1Cu1Fe1Mn1W0.5	780	1510
Al1Cr1Fe1Mo0.5Ni1	623.7	1914.1
Al1Cr1Fe1Mo0.5Ni1Ti0.25	712	2161.7
Al1Cr1Fe1Mo0.5Ni1Ti0.4	731.9	2185.1
Al1Cr1Fe1Mo0.5Ni1Ti0.5	751.7	2228.7
Al1Cr1Fe1Mo0.5Ni1Ti0.6	756.1	1314.5
Al1Cr1Fe1Mo0.5Ni1Ti0.75	766.2	618.8
Al1Co1Cr1Cu1Fe1Ni1 Mo0.4	689.3	1690
Al1Co1Cr1Cu1Fe1Ni1Mo0.6	805.3	1880
Al1Co1Cr1Cu1Fe1Ni1Mo0.8	868.4	1920
Al1Co1Cr1Cu1Fe1Ni1Mo1	875.9	1750
Co1Cr1Fe1Ni1Mo0.3	200	305
Co1Cr1Fe1Ni1Mo0.5	325	510

<b>Alloy</b>	<b>Hardness (Vickers)</b>	<b>Yield Strength (MPa)</b>
Co1Cr1Fe1Ni1Mo0.85	420	929
Al0.25 Co1 Fe1 Ni1	138	158
Al0.5 Co1 Fe1 Ni1	212	346
Al0.75 Co1 Fe1 Ni1	385	794
Al1 Co1 Fe1 Ni1	456	964
Co1 Fe1 Ni1	125	206.5
Co1 Fe1 Ni1 Si0.25	149	196
Al1 Co1 Cr1 Fe1 Nb0.1 Ni1	569	1641
Al1 Co1 Cr1 Fe1 Ni1 Ti0.5	178	2260
Al0.2 Co1 Cr1 Fe1 Mn1 Ni1	171	220
Al0.38 Co1 Cr1 Fe1 Mn1 Ni1	182	244
Al0.43 Co1 Cr1 Fe1 Mn1 Ni1	183	285
Al0.49 Co1 Cr1 Fe1 Mn1 Ni1	220	331
Al0.56 Co1 Cr1 Fe1 Mn1 Ni1	278	526
Al0.62 Co1 Cr1 Fe1 Mn1 Ni1	405	833
Co1 Cr1 Fe1 Mn1 Ni1	155.5	219
Co1 Cr1 Fe1 Mn1 Ni1 V0.5	275	620
Co1 Cr1 Cu1 Fe1 Ni1	286	230
Al1 Cu0.889 Fe0.667 Ni0.889 Ti1	516	980
Al1 Cu1 Fe1 Ni1 Ti1	516	1074
Al1 Cu1 Ni1 Ti1	537	300
Cu1 Mn1 Ni1 Zn0.333	147	215
Cu1 Mn1 Ni1 Zn0.25	109	140
Al0.053 Cu1 Mn1 Ni1	166	330
Al0.1 Co1 Cr1 Fe1 Mn1 Ni1	432	1631
Al0.3 Co1 Cr1 Fe1 Mn1 Ni1	511	1836
Al0.5 Co1 Cr1 Fe1 Mn1 Ni1	553	1932
Al0.7 Co1 Cr1 Fe1 Mn1 Ni1	622	2230
Co1 Cr1 Fe1 Ni1	168.9	163
Co1 Cr1 Fe1 Ni1 W0.2	244	335
Co0.333 Cr0.667 Fe0.667 Ni1 Ti0.2	308	586
Cr0.5 Fe0.5 Ni1 Ti0.15	335	672
Al0.333 Co0.333 Cu0.333 Fe0.333 Ni1	279.6	268
Cr1 Fe1 Ni1 Ti0.2	362.2	2297.94
Cr1 Fe1 Ni1 Ti0.3	510.3	2364.63
Cr1 Fe1 Ni1 Ti0.4	600.3	2475.41

Alloy	Hardness (Vickers)	Yield Strength (MPa)
Cr1 Fe1 Ni1 Ti0.5	709.6	2380.79
Cr1 Fe1 Ni1 Ti0.6	718.2	1923.15
Al0.562 Co0.938 Cr0.312 Fe0.312 Ni1	305.4	1129.4
Al0.581 Co0.968 Cr0.323 Fe0.323 Mo0.032 Ni1	357.3	1159.7
Al0.6 Co1 Cr0.333 Fe0.333 Mo0.067 Ni1	362.6	1250.8
Al0.6 Co1 Cr0.333 Fe0.333 Mo0.1 Ni0.967	359.7	1198.3
Co1 Cr1 Cu1 Ni1 Zn1	615	2121
Co1 Cr1 Fe1 Mn1 Ni1	435	1100
Al0.267 Co1 Cr0.667 Fe0.667 Ni0.667 Ti0.2	515	2012
Al1 Co1 Cr1 Cu1 Fe1 Ni1	551.3	1300
Al1 Co1 Cr1 Cu1 Fe1 Ni1 Mo0.2	579.2	1420
Co1 Cr1 Fe1 Ni1	135	136
Al0.214 Nb0.714 Ta0.571 Ti1 V0.143 Zr0.929	500	1965
Al0.214 Nb0.714 Ta0.714 Ti1 Zr0.929	490	1965
Al0.4 Hf0.6 Nb1 Ta1 Ti1 Zr1	500	1841
Al0.333 Nb0.667 Ta0.533 Ti1 V0.133 Zr0.667	530	2035
Al1 Mo0.5 Nb1 Ta0.5 Ti1 Zr1	591	2000
Al0.667 Nb1 Ta0.333 Ti1 Zr0.333	408	1280
Al0.3 Hf1 Nb1 Ta1 Ti1 Zr1	353	1188
Al0.5 Hf1 Nb1 Ta1 Ti1 Zr1	396	1302
Al0.75 Hf1 Nb1 Ta1 Ti1 Zr1	427	1415
Al1 Hf1 Nb1 Ta1 Ti1 Zr1	441	1489
Al0.25 Mo1 Nb1 Ti1 V1	460	1250
Al0.5 Mo1 Nb1 Ti1 V1	487	1625
Al0.75 Mo1 Nb1 Ti1 V1	517	1260
Al1 Mo1 Nb1 Ti1 V1	537	1375
Mo1 Nb1 Ti1 V1	441	1200
Al1 Nb1 Ti1 V1	448	1020
Cr1 Mo0.5 Nb1 Ta0.5 Ti1 Zr1	540	1595
Cr1 Nb1 Ti1 V1 Zr1	482	1298
Cr1 Nb1 Ti1 Zr1	418	1260
Nb0.5 Ti0.5 V1 Zr0.5	304	918
Nb1 Ti1 V1 Zr1	335	1105
Hf1 Mo0.25 Nb1 Ta1 Ti1 Zr1	395	1112
Hf1 Mo0.5 Nb1 Ta1 Ti1 Zr1	480	1317

<b>Alloy</b>	<b>Hardness (Vickers)</b>	<b>Yield Strength (MPa)</b>
Hf1 Mo0.75 Nb1 Ta1 Ti1 Zr1	492	1373
Hf1 Mo1 Nb1 Ta1 Ti1 Zr1	505	1512
Hf1 Mo1 Ta1 Ti1 Zr1	542	1600
Hf1 Nb1 Si0.5 Ti1 V1	490	1399
Hf0.333 Nb0.333 Ta0.333 Ti1 Zr0.667	301	903
Mo1 Nb1 Ta1 V1	504	1525
Mo1 Nb1 Ta1 V1 W1	536	1246
Mo1 Nb1 Ta1 W1	479.25	1137.5
Cr1 Ta1 Ti0.17 V1 W1	715	2034
Cr1 Ta1 Ti0.3 V1 W1	780	2050
Cr1 Ta1 V1 W1	715	2327
Hf0.5 Mo0.5 Nb1 Si0.1 Ti1 Zr1	442	1350
Hf0.5 Mo0.5 Nb1 Si0.3 Ti1 Zr1	494	1370
Hf0.5 Mo0.5 Nb1 Si0.5 Ti1 Zr1	524	1600
Hf0.5 Mo0.5 Nb1 Si0.7 Ti1 Zr1	580	1550
Hf0.5 Mo0.5 Nb1 Si0.9 Ti1 Zr1	640	1650
Hf0.5 Mo0.5 Nb1 Ti1 Zr1	400	1150
Hf1 Nb1 Ta1 Ti1 Zr1	341.5	1118
Mo1 Nb1 Ta1 Ti0.25 W1	478.3	1109
Mo1 Nb1 Ta1 Ti0.5 W1	481.2	1211
Mo1 Nb1 Ta1 Ti0.75 W1	495.6	1304
Mo1 Nb1 Ta1 Ti1 W1	507.5	1455
Mo1 Nb1 Re0.5 W1	473	896
Nb1 Ti1 Zr1	372	1223
Hf1 Nb1 Ti1 Zr1	351	1000
Hf0.25 Ti1 V0.5 Zr0.5	338.3	1160
Hf0.25 Nb0.125 Ti1 V0.5 Zr0.5	332.4	1115
Hf0.25 Nb0.25 Ti1 V0.5 Zr0.5	322.5	1065
Hf0.25 Nb0.375 Ti1 V0.5 Zr0.5	318.9	1025
Hf0.25 Nb0.5 Ti1 V0.5 Zr0.5	310.4	980
Nb1 Ta1 Ti1 Zr1	358	1144
Nb1 Ta1 Ti1	246	620
Nb1 Ti1 Zr1	295	956
Cr1 Mo1 Nb1 Ta1 V1 W1	996.53	3388
Cr0.286 Mo0.476 Nb1 Ta0.024 Ti0.31 V0.286	741	2680
C0.2 Mo1 Nb1 Re0.5 Ta0.2 W1	510	1074

Alloy	Hardness (Vickers)	Yield Strength (MPa)
C0.4 Mo1 Nb1 Re0.5 Ta0.4 W1	558	1144
C0.5 Mo1 Nb1 Re0.5 Ta0.5 W1	583	1202
C0.6 Mo1 Nb1 Re0.5 Ta0.6 W1	615	1241
Cr1 Fe1 Mo1 Nb1 V1	826	2663
Cr1 Fe1 Mo1 Nb1 Ti1	792	1647
Fe1 Mo1 Nb1 Ti1 V1	699	1707
Mo1 Nb1 Si0.25 Ta1 W1	567	1826
Mo1 Nb1 Si0.5 Ta1 W1	697	1883
Mo1 Nb1 Si0.75 Ta1 W1	682.6	2483
Hf1 Ti1 Zr1	211	773
Hf1 Sc1 Ti1 Zr1	233	1001
Hf1 Ti1 Y1 Zr1	241	554
Hf1 Sc1 Ti1 Y1 Zr1	256	793
Nb1 Ta0.667 Ti0.667 Zr0.333	294	822
Hf0.5 Nb0.5 Ta0.5 Ti1.5 Zr1	301	903
Al0.3 Fe1 Co1 Ni1	153	221
Al0.3 Cr0.5 Fe1 Co1 Ni1	163	233
Al0.3 Cr1 Fe1 Co1 Ni1	171	259
Al0.3 Cr1.5 Fe1 Co1 Ni1	191	294
Al0.31Cr1.7 Fe1 Co1 Ni1	229	338
Al0.3 Cr2.0 Fe1 Co1 Ni1	343	546
Al1 Co1 Cr1 Fe1 Ti0.5	943.7	1160
Al1 Co1 Cr1 Fe1 Ti0.5 Ni1	761.7	1990
Al1 Co1 Cr1 Fe1 Ti0.5 Ni1.5	723.6	1920
Al1 Co1 Cr1 Fe1 Ti0.5 Ni2.0	612.2	1800
Al1 Co1 Cr1 Fe1 Ti0.5 Ni2.5	566.1	1410
Al1 Co1 Cr1 Fe1 Ti0.5 Ni3.0	503.2	1090
Al0.5 Co1 Cr1 Cu1 Fe1 Ni1	399	1292
Zr1.0 Ti0.86 Nb0.57 Al0.33 Ta0.14	311	850
Zr1.0 Ti0.86 Nb0.57 Al0.33 V0.14	314	848
Ni1 Co1 Fe1 Al1 Ti1	216	557
Al0.12 Cr0.45 Fe1 Mn0.27 Mo0.03 Ni1 Ti0.12	358.5	720
Al0.12 Cr0.45 Fe1 Mn0.24 Mo0.06 Ni1 Ti0.12	411	747
Al0.12 Cr0.45 Fe1 Mn0.21 Mo0.09 Ni1 Ti0.12	419	772
Al0.12 Cr0.45 Fe1 Mn0.18 Mo0.12 Ni1 Ti0.12	439.2	905
Al0.12 Cr0.45 Fe1 Mn0.15 Mo0.15 Ni1 Ti0.12	566.6	1120

<b>Alloy</b>	<b>Hardness (Vickers)</b>	<b>Yield Strength (MPa)</b>
Hf1 Nb1 Ta1 Zr1	571	2310
Nb1 Ta1 Ti1 V1	427.9	1108
Al0.15 Cr0.5 Cu0.25 Fe0.5 Ni1	107	62
Al1 Nb1 Ti1 Zr1	420	1544
NbTiVZr	335	1105
CrNbTiZr	418	1260

# **Pacific Northwest National Laboratory**

902 Battelle Boulevard  
P.O. Box 999  
Richland, WA 99354

1-888-375-PNNL (7665)

***[www.pnnl.gov](http://www.pnnl.gov)***